

EUROLIFT Test Case Description for the 2nd High Lift Prediction Workshop

R. Rudnik¹, K. Huber², and S. Melber-Wilkending³
 DLR, German Aerospace Center, 38108 Braunschweig, Germany

The paper describes the experimental evidence for the DLR-F11 high lift configuration to be used within the context of the 2nd phase of the AIAA High Lift Prediction Workshop. The model geometry is representative for a wide-body commercial aircraft. For the present purpose a wing/body combination is considered with a continuous slat and flap system in landing setting. Slat and flap are intersecting with the fuselage in order to suppress side edge interference effects and their aerodynamic impact on maximum lift. A CAD model in various degrees of detail has been refurbished, serving as the common geometrical basis for the scheduled CFD investigations. Experimental data of the European project EUROLIFT for low and high Reynolds number conditions have been made available, making use of the same wind tunnel model. The data for low Reynolds numbers have been gathered in the Low Speed Wind Tunnel of Airbus in Bremen, B-LSWT, Germany, while the high Reynolds-number data have been measured in the European Transonic Windtunnel, ETW, under cryogenic conditions. The Reynolds numbers between both datasets differ by an order of magnitude. In addition to force and moment data, which are available from both wind tunnel tests, a comprehensive validation database is available of the tests in the B-LSWT. The experimental data comprise oil flow pictures, transition information by hotfilms and infrared thermography, as well as PIV velocity data in various locations of the F11 configuration for a sample of angles of attack up to and beyond maximum lift. The main features of the experimental evidence are analyzed, comparing pressures and forces for low and high Reynolds number conditions. Examples of the oil flow pictures, transition information, and off-body velocity data are presented and briefly discussed.

Nomenclature

A	= reference area	<i>greek symbols</i>
b	= wing span	α = angle of attack
C_p	= pressure coefficient	δ_f = flap deflection angle
C_L	= total lift coefficient	δ_s = slat deflection angle
C_D	= total drag coefficient	Λ = aspect ratio
c	= chord length	λ = taper ratio
dct.	= drag count (0.0001)	η = normalized span coordinate
FTF	= Flap Track Fairing	
F&M	= Forces and moments	
h	= height	subscripts
HF	= Hotfilm	f = flap
lct.	= lift count (0.01)	fu = fuselage
M	= Mach number	max = maximum of a specific quantity
IR	= Infrared Thermography	ref = reference quantity

¹ Head Transport Aircraft Branch, Institute of Aerodynamics and Flow Technology, Lilienthalplatz 7, 38112 Braunschweig, Germany, Member AIAA

² Research Engineer, Transport Aircraft Branch, Institute of Aerodynamics and Flow Technology, Lilienthalplatz 7, 38112 Braunschweig, Germany

³ Research Engineer, Transport Aircraft Branch, Institute of Aerodynamics and Flow Technology, Lilienthalplatz 7, 38112 Braunschweig, Germany

PIV	= Particle Image Velocimetry	s	= slat
Re	= Reynolds number based on cref	∞	= free stream value
s	= half span	tot	= total quantity
w	= width		
T	= temperature		

I. Introduction and Background

The successful first AIAA High Lift Prediction workshop (HiLiftPW-1) proved the request and demand for a sustained international CFD validation exercise for 3-dimensional high lift configurations. For HiLiftPW-1, the NASA trapezoidal wing has been selected as a reference configuration, featuring a generic semi-span, three element high lift wing configuration with a body pod¹. The wing has a comparatively low aspect ratio of AR= 4.56, it is untwisted and has no dihedral. The considerations to identify a reference configuration for the 2nd AIAA High Lift Prediction Workshop were driven by the request to take a more realistic high lift configuration into account, while avoiding to include the full complexity of the interference phenomena of a wing mounted engine or nacelle on the high lift aerodynamics. As an available experimental database has been a prerequisite, the DLR-F11 wing/body high lift configuration and the corresponding windtunnel test data in the framework of the EC-project EURLOFT² have been proposed as a suitable test case for the 2nd workshop phase by the organizing committee of the High Lift Prediction Workshop. Out of the four complexity stages of the F11 model³, the wing/body configuration with a full span flap and slat in landing setting is considered for HiLiftPW-2. The windtunnel data have been recorded in the low speed wind tunnel of Airbus-Deutschland, B-LSWT, as well as in the European Transonic Windtunnel ETW. The atmospheric tests in the B-LSWT at a chord Reynolds number of $Re = 1.4 \times 10^6$ provide the more comprehensive experimental database with forces, pressure distribution, off-body PIV data, oil flow pictures, and transition information by hotfilms and infrared thermography. The DLR-F11 configuration in the set-up for the HighLiftPW-2 studies in the B-LSWT is shown in Fig. 1



Fig. 1 DLR-F11 model in the B-LSWT throughout the EUROLIFT test campaign

The test results under cryogenic conditions at Reynolds number of $Re = 15 \times 10^6$ are representative for flight Reynolds numbers and cover forces and wall pressure distributions, as well as limited tuft video information.

The paper describes geometrical details of the F11 high lift configuration, the CAD model and various options of model details, as well as the experimental evidence for the respective configuration and the two wind tunnel facilities. A proposal for benchmark flow conditions is presented as well as a critical assessment of the measured data and their consistency

II. DLR-F11 Configuration Specification for the High Lift Prediction Workshop

The baseline model for the EUROLIFT investigations described in more detail in Ref. 3 and 4 is representative for a commercial wide-body twin-jet high lift configuration. The layout and geometry has been defined by Airbus-Deutschland, denoted as KH3Y geometry. The windtunnel model is constructed and manufactured by DLR and denominated DLR-F11 model. The cruise configuration is equipped with a baseline and a modified leading edge. The baseline wing has a comparatively sharp leading edge design, resulting in unsatisfying low speed high lift characteristics especially at low Reynolds numbers. Therefore an alternative leading edge with a nose modification has been designed. The modified nose design with a small nose droop considerably improves the maximum lift behavior. The nose droop design forms also the geometrical basis for all high lift configurations of the KH3Y-configuration. The main dimensions of the model are listed in table 1:

Table 1: Main dimensions of DLR-F11 (KH3Y) model

half span, s	[m]	1.4
wing reference area, $A/2$	[m ²]	0.41913
reference chord, c_{ref}	[m]	0.34709
aspect ratio, Λ	[-]	9.353
taper ratio, λ	[-]	0.3
¼ chord sweep, ϕ_{25}	[°]	30
fuselage length, l_{Fu}	[m]	3.077

The high lift system consists of a leading edge slat and a trailing edge Fowler flap. The slat is subdivided into three parts. The elements are interconnected laterally by latches. The slat is continuously extending up to the wing tip. The local relative chord ranges from about 10 % at the inboard pressure section (PS1) to nearly 24% chord at the most outboard pressure section (PS11). The Fowler flap also consists of three parts. The first one extends up to the wing kink, and the second one up to 71% half span. The third element extends up to the wing tip. It can be interchanged against a flaperon. For a representative wing section at 68% half span the slat has a local chord length of 17.7% and the flap of 27.6%, respectively. The high lift system can be mounted in two take-off settings and one landing setting. For the present studies, only the landing setting is considered. The flap can be mounted in several fixed window positions. The reference setting for the landing configuration is denoted as WP 9. The device rigging specifications in terms of deflection, gap, and overlap for WP 9 are listed in table 2.

Table 2: Specification of the DLR-F11 model in landing configuration, WP 9

slat deflection angle, δ_s	[°]	26.5
slat gap, g_s / c_{ref}	[-]	0.014
slat overlap, o_s / c_{ref}	[-]	-0.008
flap deflection angle, δ_f	[°]	32.0
flap gap, g_f / c_{ref}	[-]	0.010
flap overlap, o_f / c_{ref}	[-]	0.006

For all experiments of the EUROLIFT projects the model is tested as a half model to make use of the larger scale compared to full model tests. The model is mounted on a Peniche. The KH3Y model consists of a metal main wing structure with detachable leading and trailing edges to enable various high lift devices to be fitted. The fuselage shells are manufactured from carbon fiber. Fuselage as well as the Peniche incorporate labyrinth seals adjacent to each other. The Peniche is equipped with brush strips adjacent to the test section wall. The effective height of the Peniche and the seals in the wind tunnel amounts to 0.101m. The high lift devices have been manufactured to fit gapless in spanwise direction for the take-off setting 2. Consequently, also the pressure sections of slat and flap are in-line with the fixed wing pressure sections for this setting. To seal the high lift devices in landing setting, aluminum alloy tape was used. At the kink joint a carbon fiber piece is used to close the flap joint gap. A roughness

band of 5 mm width is attached to the fuselage 30 mm downstream of the fuselage. The transition strip is made of carborundum K80. All other components are testes without any transition fixing.

In EUROLIFT (I) the model has been used in a wing/body configuration equipped with full-span devices and alternatively a part span flap with retracted flaperon. For the present investigations, only the full-span flap configuration is considered. The slat is attached to the main wing using 7 slat tracks. The flaps are mounted with 5 flap tracks and a fixing of the inner flap edge at the fuselage. The flap tracks are covered by flap track fairings. The high lift devices directly intersect with the fuselage. The high lift wing is equipped with 487 pressure taps in 10 pressure sections (PS), as illustrated in Fig. 2.1. Pressure section 3 is not available for the high lift model.

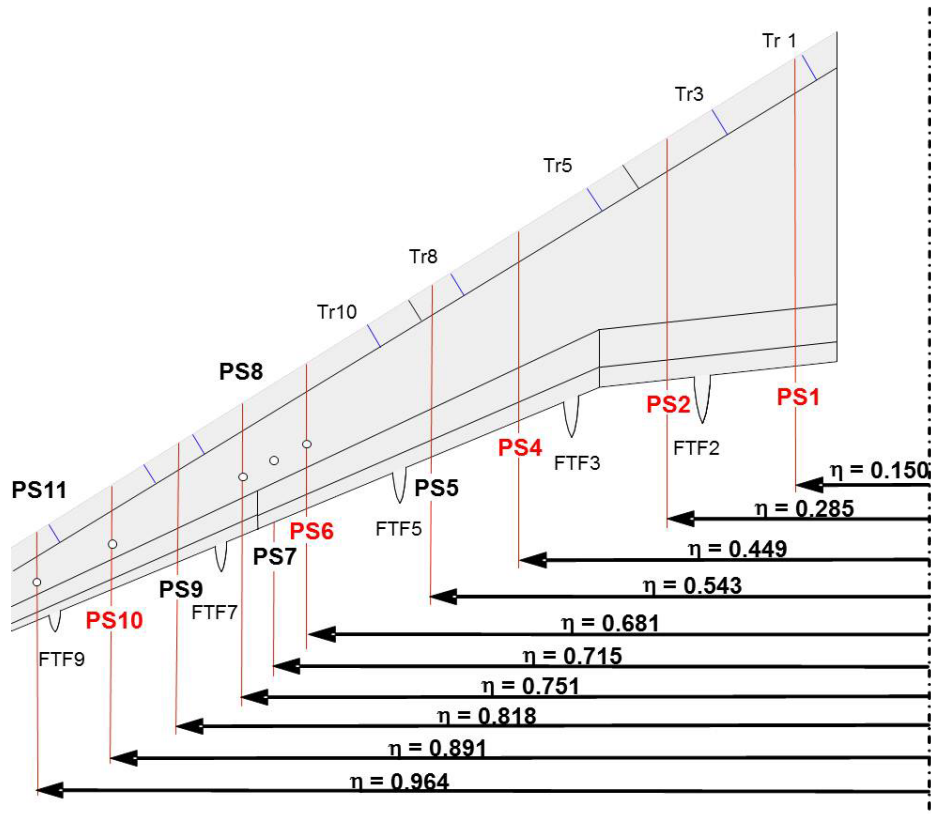


Fig. 2.1. DLR-F11 high lift configuration; location of pressure sections

The CAD data are provided with different degrees of details of the model. The baseline model, Stage 0-1, consists of the wing/body elements only, featuring the fuselage with its belly fairing and the high lift wing with slat and flap with flap track fairings, but without the slat brackets. For this configuration as for the other ones under consideration for HighLiftPW-2, flap and slat intersect laterally with the fuselage. In order to realize this intersection for different flap positions a plain functional surface had to be added to the fuselage at the rear flap/fuselage intersection, see Fig. 2.2. Including the functional surface in the CAD model leads to configuration Stage 0-2. As some grid generation packages might run into trouble when incorporating this feature CAD models with and without this surface are provided.



Fig. 2.2. Plain functional surface at the flap/fuselage intersection of the DLR-F11 model; windtunnel model on the left, CAD model the right hand side

Due to the comparatively high resolution pressure instrumentation of the model for the given dimensions, the pressure tube bundles had to be attached externally to the slat tracks for their routing into the wing. Throughout the test campaigns in the B-LSWT variations with and without the pressure tube bundles as shown in Fig. 2.3 have been conducted.

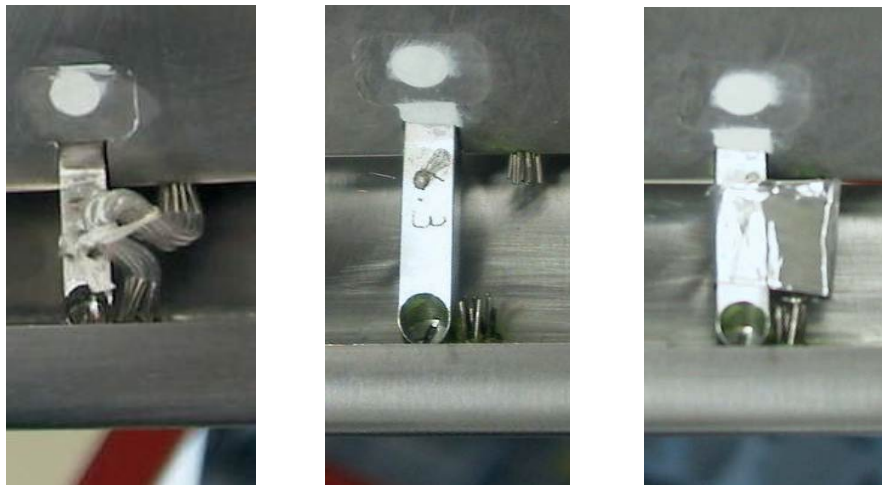


Fig. 2.3. Detail of the slat tracks with and without externally attached pressure tube bundles and with a simplified replacement body

The pressure tube bundles revealed a distinct influence on $C_{L_{max}}$ for the landing configuration in the order of 5 lcts.. Therefore, two more CAD models are provided, one including slat tracks and the other including slat tracks and a geometrical representation of the pressure tube bundles. Fig. 2.4 shows the most complex CAD description of the DLR-F11 high lift configuration from different perspectives in the most complex version.

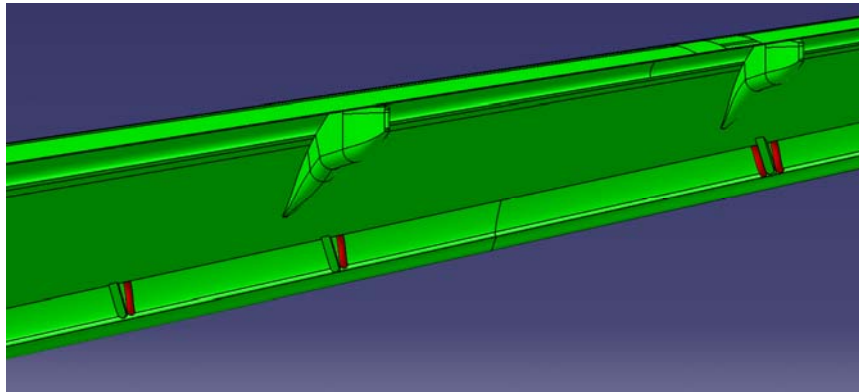
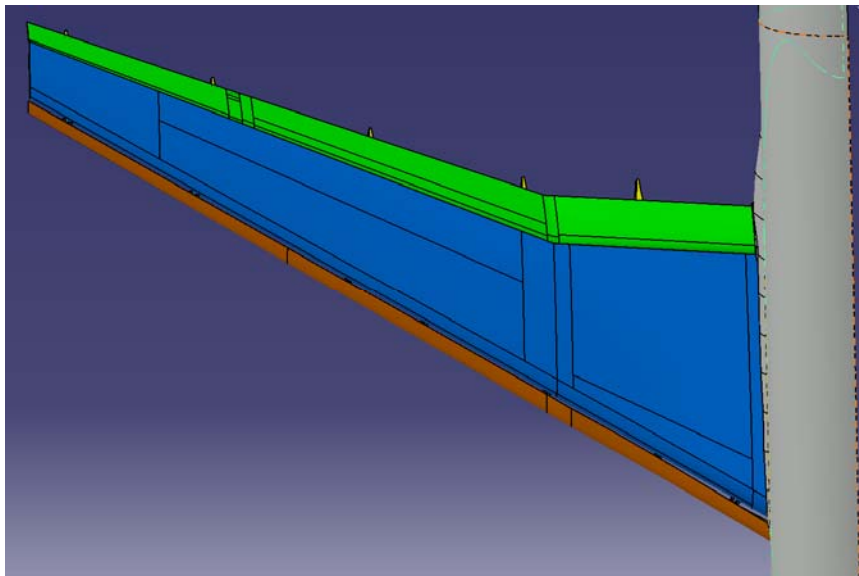
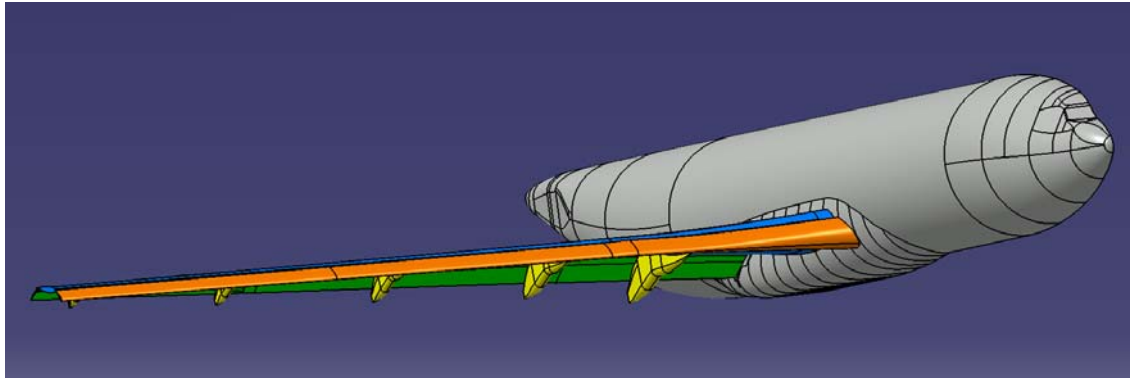


Fig. 2.4. CAD model for the DLR-F11 high lift configuration including all geometric details

III. Experimental Set-Up and Facilities

The experimental data presented in this context have been gathered on the DLR-F11 windtunnel model in the low speed wind tunnel of Airbus-Deutschland, B-LSWT, in Bremen, Germany, as well as in the European Transonic Windtunnel ETW in Cologne, Germany, as part of the EUROLUIFT (I) project⁵.

A. Low Speed Wind Tunnel, B-LSWT

The AIRBUS low speed tunnel B-LSWT in Bremen has an open Eiffel-type circuit with a closed test section and a contraction ratio of 4.82:1. The tunnel is installed in a hall that houses the return circuit. The operating speed range is from 5 m/s to 80 m/s. The test section is 4.45 m in length, with a cross section measuring 2.1 m x 2.1 m. The floor and ceiling of the test section are each equipped with a turntable. The turntables can rotate either separately to each other, or simultaneously. The model is attached to the turntable in the ceiling of the test section as depicted in Fig. 3.1, left.



Fig. 3.1. DLR-F11 model in the B-LSWT in the set-up for pressure measurements (left), PIV measurements (center), and Infra Red thermography (right)

Along the sidewalls several glass windows are inserted to allow optical access. An additional window set is mounted in the floor turntable, visible in the left photo in Fig. 3.1.

For all tests described in this paper the onflow velocity is 60 m/s. The resulting Reynolds number defined by the wing's mean aerodynamic chord is $Re_c = 1.35 \times 10^6$. The nominal Mach number amounts to $M = 0.175$. The tests in the B-LSWT have been split in two phases. An angle of attack range between -4° and 21° is covered by the measurements either in continuous mode or in pitch pause mode with a reduced so called short sequence of angles of attack.

During the first phase in July 2001 basically forces, moments, pressure distributions, oil flow pictures, and tuft videos have been recorded for various settings of the high lift devices. The following second phase in August and September 2001 focused on PIV flowfield measurements, transition detection via hotfilms and infrared thermography, as well as boundary layer measurements using miniature boundary layer rakes. Fig. 3.3 shows the locations of the PIV-planes and the hot films in the planform view on the F11-model.

To reduce / eliminate reflections of the model surface For the PIV measurements, special means were necessary as the model wing was made from polished steel for cryogenic testing. For this purpose a thin, black, smooth, self-adhesive foil has been applied to the model beneath the three PIV-sections, see in Fig. 3.1, center photo.

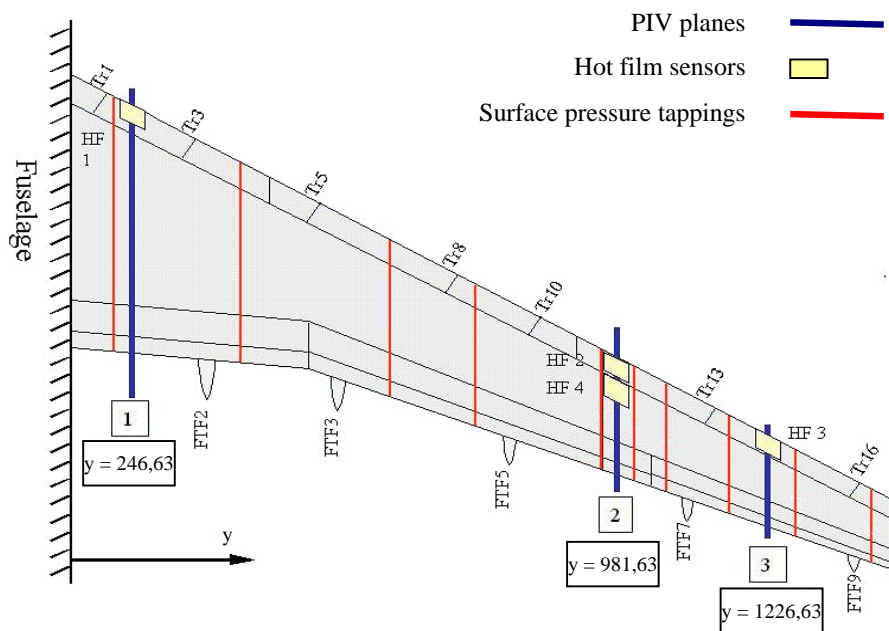


Fig. 3.2. Location of the test equipment for the second phase of the windtunnel test in the B-LSWT

The PIV measurements are conducted in a two-dimensional manner in three planes. The planes are oriented in line of flight and parallel to the tunnel floor or model symmetry plane, respectively. Their spanwise position is also shown in Fig 3.2. The locations of the green laser light sheets is depicted in Fig. 3.3.

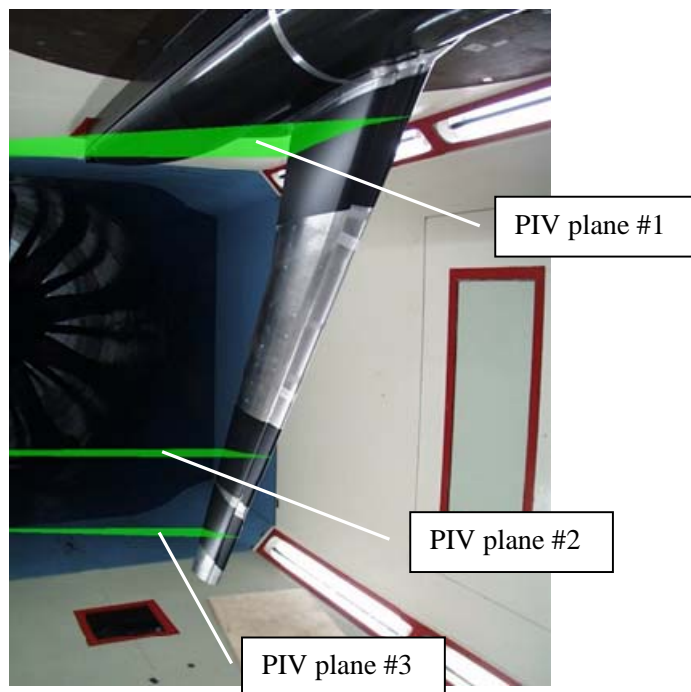


Fig. 3.3. Orientation of PIV-planes in B-LSWT set-up

The thickness of the light sheet at the wing surface was approximately 2 to 3 mm. For plane 1, a periscope mirror system has been devised that could be attached to the inside wall of the test section. For the landing configuration, 2-component PIV measurements have been carried out for PIV-planes 1, 2, and 3. For plane 2, also stereo (3-component) PIV was carried out. PCO 12-bit CCD cameras were used, mounted under the tunnel on a frame. The camera frame was constructed from aluminium X-95 profiles. This frame allowed more than one camera to be positioned at a time and was attached firmly to the turntable in the tunnel floor, so that the cameras could rotate with the turntable allowing PIV results to be obtained for an incidence polar with relative ease. For seeding a mist of special DEHS oil has been sprayed into the incoming airflow with compressed air via two seeding generators, placed on the floor of the wind tunnel hall, upstream of the tunnel intake. The size distribution of the particles is approximately bell-shaped, with a modal diameter slightly bigger than 1 μm .

In each spanwise plane, the cameras were aimed at various chordwise positions or so-called windows, which are shown in Fig. 3.4. The windows have been designated by alphabetical characters in each plane. The experimental set-up is described in Ref. 6 and 7.

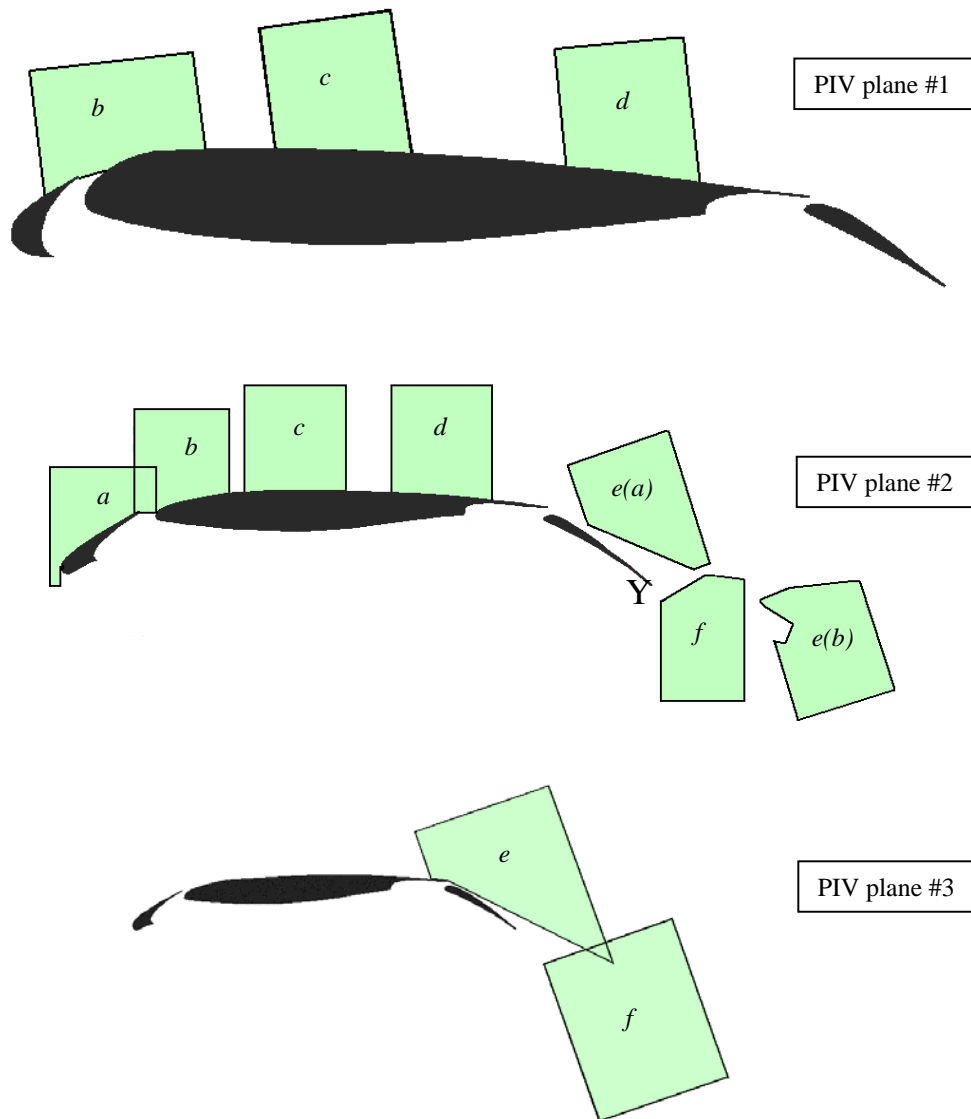


Fig. 3.4. Windows in PIV planes # 1,2, and 3

To assign position information to the velocity field at distinct points measured in each of the windows, a local coordinate system has been defined for each PIV plane. The origin is located at the leading edge of the deployed slat in each of the individual planes. A geometrical grid defines the distinct points in each of the windows. For the use in the HiLiftPW-2 context, the data have been transformed into the global coordinate system used for the CFD studies. In some areas of the windows, the PIV-information is not available, as the wing dihedral lead to a shadowing of parts of the windows close to the wing surface.

As the cameras were fixed outside the model, effects of static aeroelastic deformation have to be estimated and taken into account by correcting the calibrated locations of the velocity information with wind-off. For each combination of high lift configuration and model incidence, corrections for the aeroelastic shift of the wing have been estimated. Corrections of about ± 0.5 mm have been applied to the raw PIV images.

Results of the boundary layer probe measurements are not available for the present studies.

Oil flow pictures have been taken in the B-LSWT as well, making use of a special illumination. For this purpose all pressure sections have been covered by tape in order to prevent intrusion of the oil into the taps and underlying pressure tubes. A broad variety of overall pictures and close-ups have been taken of the upper and lower wing surface. Representative oil flow pictures for three angles of attack have been selected, namely for $\alpha = 7^\circ$, 18.5° , and 21° .

IR on upper and lower wing surface are available. For the infrared thermography three areas of the fixed wing and the slat have been coated by white thin foils, Fig. 3.1, right photo, to provide a thermal insulation of the metal surfaces and to avoid the typical reflections, which appear when metallic objects are scanned with infrared light. As for the PIV images an inboard, midboard and outboard area of the wing is coated, with the midboard section lying further inboard than the intermediate section of the PIV measurements. For the IR-measurements the metal slat has been exchanged against a CFRP (Carbon Fibre Reinforced Plastics) slat.

In addition to the transition detection by IR-thermography, hotfilm (HF) measurements have been carried out for the low Re-Number conditions, because especially here transitional effects are supposed to have a distinct impact on the aerodynamic performance. As can be seen in Fig. 3.2, hotfilm arrays are placed in three sections on the slat (HF1 to HF3) at the same spanwise position as the PIV planes are located. For the middle section at $y = 981.63$ mm, also the fixed wing leading edge is equipped with a hotfilm array (HF4). The same CFRP-slat as for the PIV measurements is also used for the hotfilm measurements. The HF-arrays are flush mounted on the slat surface in shallow pockets inserted in the slat surface. The edges of the hotfilm on the fixed wing leading edge are glued on top of the wing surface with the edges smoothed out with filler. As shown in Fig. 3.5, the electrical wires are routed in spanwise direction, covered by tape.



Fig. 3.5. Hotfilm arrays on the slat and the fixed wing leading edge at section HF2

23 signals are recorded for HF-array 1 on the slat, 21 signals for slat array 2, and 17 signals for slat array 3. For array 4 on the fixed wing, 24 signals are recorded. The signals have been recorded for a period of 0.5 sec, and 2 sec, respectively.

The onflow conditions of the low Reynolds number case is given in table 3. An overview of the experimental evidence is shown in table 4.

Table 3: B-LSWT onflow conditions for the test with the DLR-F11 model in landing configuration,

B-LSWT run no.		29293
Mach number (av.)	[-]	0.175
Reynolds number (av.)	[-]	1.35×10^6
Total pressure, P_{tot} (av.):	[Pa]	100.70×10^3
Total Temperature, T_{tot} (av.)	[K]	298.66
α -range	[°]	0.04 - 20.99

Table 4: Overview of data availability in the B-LSWT for the test with the DLR-F11 model in landing configuration

α	F&M	C_p	Oilflow	Hotfilm	IR	PIV	Tufts
0.04°	x	x		x	x		Video Tape
6.99°	x	x	x	x	x	x	
11.98°	x	x		x	x	x	
14.00°	x	x		x	x		
16.00°	x	x		x	x	x	
17.00°	x	x		x	x		
18.00°	x	x		x	x		
18.49°	x	x	x	x	x	x	
19.00°	x	x		x	x		
20.00°	x	x		x	x		
20.99°	x	x	x	x	x	x	

B. European Transonic Windtunnel, ETW

The European Transonic Windtunnel has a closed aerodynamic circuit with a Mach number range from $M = 0.15$ to 1.3. The test section is 8.73 m long with a cross section of 2.00 m height, and 2.40 m width. For the low speed tests it is operated with closed slots in the tunnel walls. The model set-up is the basically same as in the B-LSWT, thus, the model is mounted from the ceiling of the test section. In Fig. 3.6 the model is shown in the preparation hall underneath the test section of ETW.

The test data under consideration have been collected during a test campaign in the ETW in the summer of 2002. In this campaign the data for configuration Stage 0, corresponding to the wing/body configuration as provided for the High Lift Prediction Workshop, have been measured with a Reynolds-number range from $Re = 1.5 \times 10^6$ up to 15×10^6 . These Re-number variations are established by a combination of total pressure and total temperature settings for a Mach number of $M = 0.2$. The total temperature is varying from 300 K down to 115 K, while the total pressure varies from 1.1 bar up to about 2.6 bar for the highest Re-number of 15×10^6 . Reynolds number scaling effects for this Mach number and various Reynolds numbers have been discussed for the DLR-F11 configuration in different complexity stages including engine/airframe interference effects in Ref. 3 and 4.



Fig. 3.6. DLR-F11 Model in the preparation hall of ETW

For the test case in the High Lift Prediction Workshop 2, data from tests with a lower Mach number of $M = 0.176$ are selected in order to have a direct link to the onflow conditions in the B-LSWT. Although this Mach number is at the lower limit of the tunnel operational boundaries, it provides the opportunity to avoid any Mach number effects when comparing the low and high Reynolds number conditions. Therefore, experimental data for an onflow Mach number of $M = 0.176$ is selected in the present context in contrast to the Mach number of $M = 0.2$ analyzed in Ref. 3 and 4. Given the small difference between $M = 0.176$ and 0.2 and the comparatively low level, the Mach-number is supposed to have a negligible influence on the high lift aerodynamics. In order to cover the same Reynolds number range from $Re = 1.5 \times 10^6$ up to 15×10^6 , the total temperature in the ETW tests is varying from 300 K down to 115 K, while the total pressure varies from 1.1 bar up to about 3 bar for the highest Re-number of 15×10^6 . The onflow conditions of the high Reynolds number case is given in table 5. For the use in the framework of the High Lift Prediction Workshop 2, the highest Reynolds number of $Re = 15 \times 10^6$ is selected as a database to be compared to the low Reynolds-number data of the B-LSWT.

Table 5: ETW onflow conditions for the test with the DLR-F11 model in landing configuration,

ETW run no.		238
Mach number (av.)	[-]	0.176
Reynolds number (av.)	[-]	15.1×10^6
Total pressure, P_{tot} (av.):	[Pa]	301.56×10^3
Total Temperature, T_{tot} (av.)	[K]	114.7
α -range	[°]	-3.20 - 24.24

An overview of the experimental evidence of the ETW test is shown in table 6. Reference polar 238 has been measured in continuous mode with data recorded for more than 200 angles of attack. Out of these, the angles of attack corresponding to the low Reynolds number conditions of the B-LSWT have been selected and refurbished.

Table 6: Overview of data availability in the ETW for the test with the DLR-F11 model in landing configuration

α	F&M	C_p	Tufts
0.01°	x	x	Video Tape
7.04°	x	x	
11.97°	x	x	
13.98°	x	x	
15.99°	x	x	
16.98°	x	x	
18.00°	x	x	
18.49°	x	x	
19.00°	x	x	
20.02°	x	x	
20.95°	x	x	

IV. Experimental Evidence from EUROLIFT Wind Tunnel Studies

The experimental results of both wind tunnels featuring a difference in Reynolds number of about an order of magnitude will be discussed in separate sections starting with the more comprehensive database for low Reynolds numbers in the B-LSWT.

A. Experimental Evidence of the Low Speed Wind Tunnel, B-LSWT

Based on the different measurements on the F11 configuration in the B-LSWT, selected examples of the different datasets shall be highlighted in order to provide an aerodynamic understanding of the high lift performance of the F11 wing/body configuration under these onflow conditions with a special focus on $C_{L,max}$. The analysis of the data will start with force and moments plots. Then pressure distributions will be presented. After this, selected oil flow pictures will be shown to complete the analysis of the stall behavior. PIV-data are used to provide a certain understanding of the off-body flowfield. The analysis of the low Reynolds-number results will be closed by a presentation of studies of the transition phenomena.

Forces and Pitching Moments

As described in the previous chapter, the reference for the use of the data of the B-LSWT is run 29293. The onflow parameters are listed in table 3. Fig. 4.1 shows the corresponding lift curve, drag polar, and pitching moment distribution for the positive angle of attack range. $C_{L,max}$ of 2.62 is reached at an angle of attack of $\alpha(C_{L,max}) = 19^\circ$. The lift breakdown after maximum lift is smooth. Taking into account that the angle of attack steps are quite large in the lower lift range, it can be noted that a deviation from the linear lift slope starts already at about $\alpha = 10^\circ$ for the low Reynolds-number condition. The red symbols indicate the angles of attack, which will be analyzed in more detail in the following. They are chosen to investigate the linear lift range at moderate angles of attack, representative for the operational conditions, a value close to maximum lift, and a post maximum lift angle of attack in order to analyze the separation growth. The drag polar reveals a minimum drag in this part of the polar of about $C_{D,min} = 0.1$ and a maximum value at post-maximum lift conditions of about 0.45. The resulting best L/D of the data considered are reached at the lower angles of attack where separation isn't affecting the lift generation with a maximum of $L/D \sim 11.4$ occurring at $\alpha = 6.99^\circ$. The strong negative pitching moment at $\alpha = 0^\circ$ tends to decrease (less nose down) progressively with increasing lift. Beyond lift breakdown, pitching moment is slightly becoming more negative again for the highest angle of attack of $\alpha = 21^\circ$.

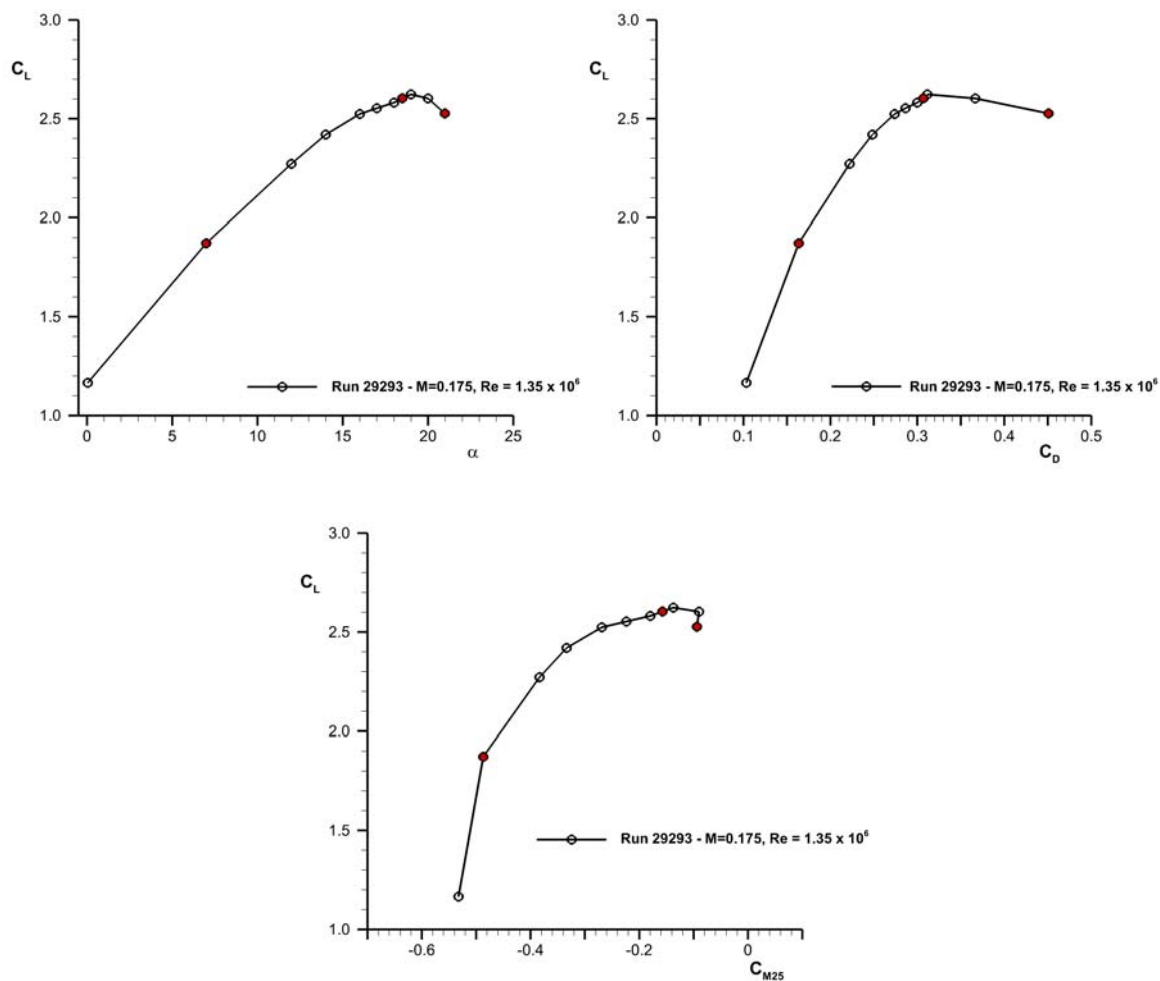


Fig. 4.1. Lift, drag, and pitching moment for the reference dataset for low Reynolds-number conditions

Short and short-medium term repeatability has been investigated. Fig. 4.2 shows corresponding plots for the lift curve, the drag polar, and pitching moment. All lift curves have been measured during the first phase of the tests. Runs 29293 and 29292 have been recorded on one day during the early phase, runs 29318 and 29319 on a single day at a later stage of the first phase with comprehensive variations in the high lift device setting in between. As can be seen by the couples of measurements with the same color, very good short term repeatability is achieved for high lift half model measurements. The deviations in lift at the angle of attack of $\alpha = 19^\circ$ are below 0.1%. For drag the differences are below 0.2%, which translates into about 6 and 4 dcts., respectively. When looking at the graphs it has to be noted the number of angles of attack differs for the polar pairs of the same color. The differences in pitching moment are higher, as this is known to be a much more sensitive quantity than lift. The difference in pitching moments is below 1% for both pairs of results.

In contrast to this, the differences are considerably higher when comparing the black and the green graphs, that is, results that have been recorded with model modifications in between. Looking again at the data for $\alpha = 19^\circ$, the differences between e.g. Run 29293 and 29318 amount to 1.1%, 0.8%, and 14% in lift, drag, and pitching moment, respectively. These differences are considered unusual high for repeats within one campaign. Thorough studies have been conducted revealing that either difficulties in the required precise adjustment of the high lift settings for this specific model and its adjustable brackets could be a potential reason, or the surface quality of the model during the initial phase of the tests, taking into account the sensitivity against transitional effects for the low Reynolds number

conditions. The model has been repeatedly cleaned and polished throughout the various tests phases. In summary, this underlines the sensitivity of the data against slight changes in environmental or model conditions and adjustments. The difference in maximum lift amounts to 3 lts.. Note, that when later-on effects of model instrumentation will be discussed, the corresponding high lift performance will be related to the runs 29318 as this is the relevant reference for investigations using HF, PIV or oil flow.

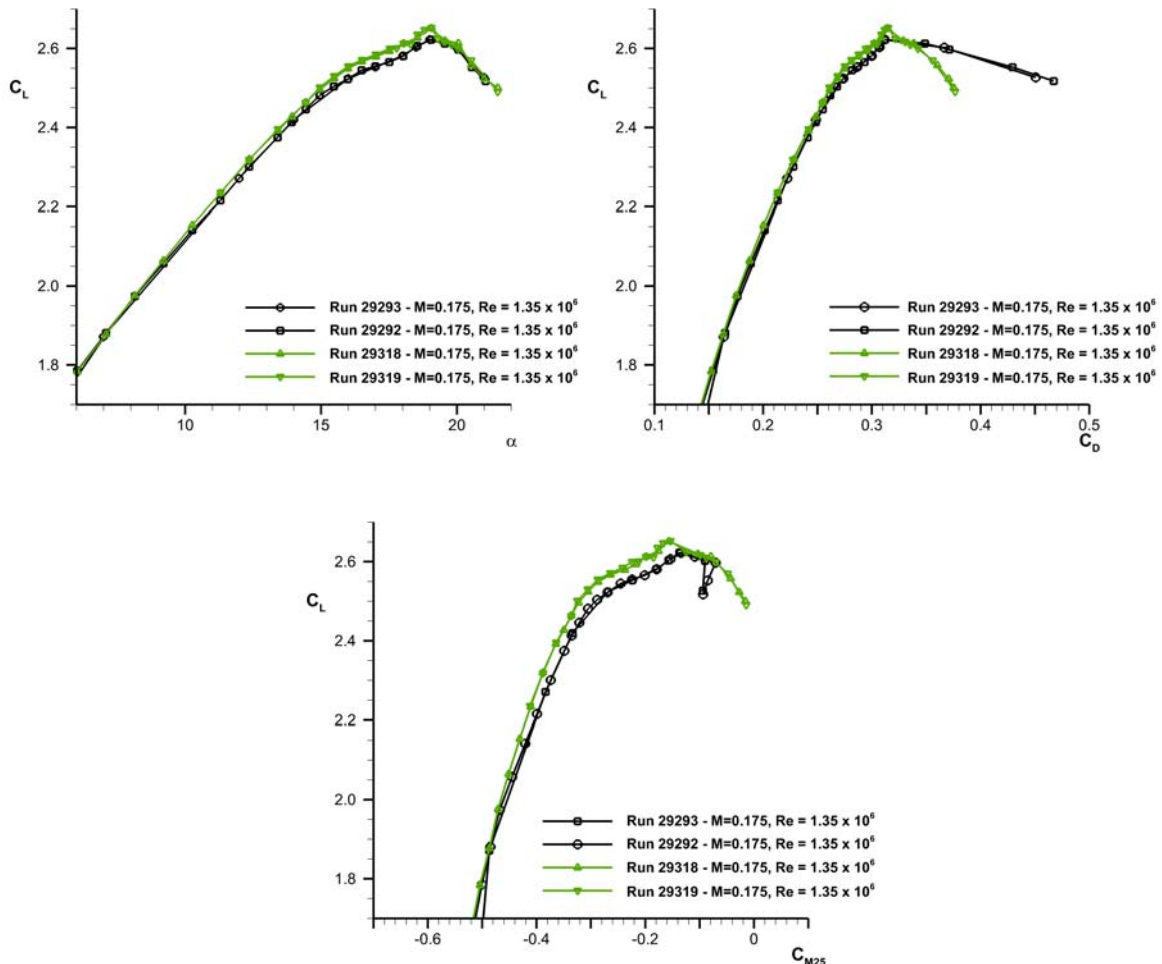


Fig. 4.2. Short and medium turn repeatability for the reference dataset for low Reynolds-number conditions

Pressure Distributions

In order to investigate the lift generation and breakdown 10 pressure distributions are available. Fig. 2.1 shows the spanwise locations. Note that PS 3 is omitted due to the optional engine integration.

Pressure distributions in section 4 at $\eta = 0.449$ and section 10 at $\eta = 0.891$ are depicted on all elements of the high lift wing in Fig. 4.3 and Fig. 4.4 for the three reference angles of attack, indicated in the lift curve in Fig. 4.1. Pressure taps with missing or erroneous signals are omitted in the line interpolation. The chordwise coordinate is normalized with the respective element chordlength. Note, that different scales at the ordinate are used for the three elements.

For PS 4 the suction level on the slat is monotonously increasing from a very flat and low level at $\alpha = 7^\circ$ to distinct suction peaks of up to $cp \sim -12$ at post $C_{L,max}$ conditions. The fixed wing shows similar trends with the most notable difference, that the suction level in the front part of the wing isn't basically changing from $\alpha = 18.5^\circ$ to $\alpha = 21^\circ$. The flap features contrary trends as the flat, namely a continuously decreasing suction level with increasing angle of attack.

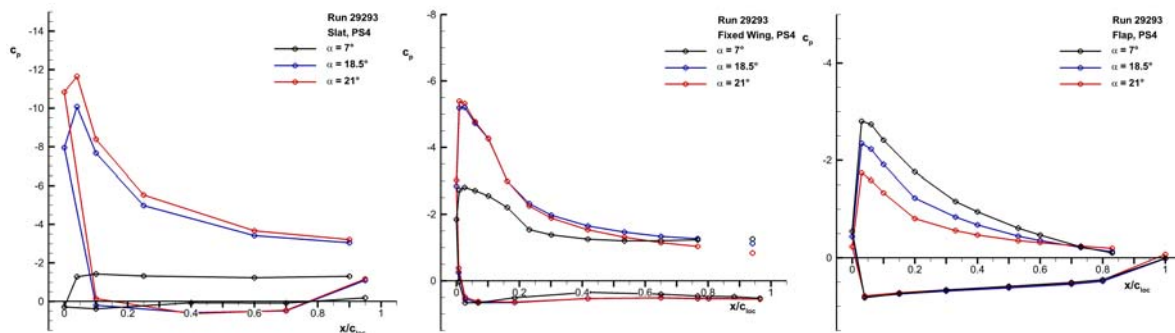


Fig. 4.3. Midboard pressure distribution at different angles of attack for low Re-number conditions

The pressure distributions at the outboard sections PS 10 in Fig. 4.4 show the same trends on all three elements. The suction levels at the slat are considerably lower than at the midboard section. In contrast to section PS4, the fixed wing is higher loaded at the outboard section. Unfortunately, numerous pressure tab information has to be omitted in the aft part of the flap suction side and the front part of the pressure side limiting the value of this section.

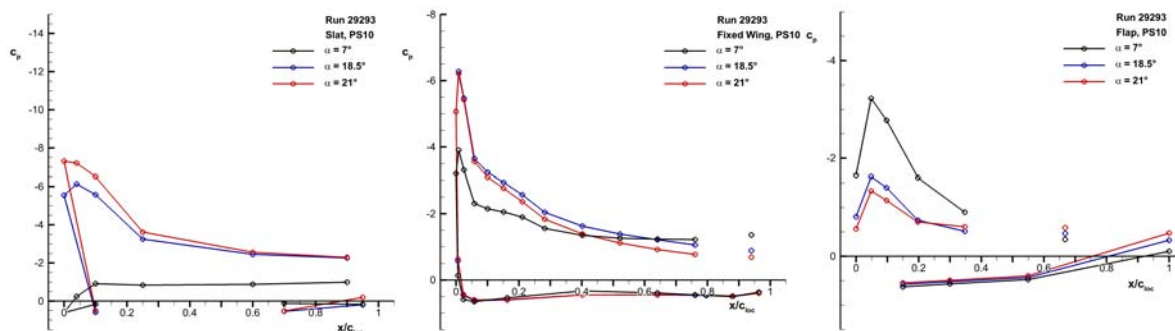


Fig. 4.4. Outboard pressure distribution at different angles of attack for low Re-number conditions

In order to assess the spanwise development of the lift generation, especially the lift breakdown, pressure sections PS1, PS2, PS4, PS6, and PS 10 are plotted in a three-dimensional view in Fig. 4.5 for $\alpha = 18.5^\circ$ and $\alpha = 21^\circ$, respectively. For the slat, the observation of Fig. 4.3 and Fig. 4.4 has been that the suction level is increasing beyond maximum lift. This observation is valid for the other sections, too. PS 4 is characterized by the highest suction peaks, while the inboard section PS 1 at 15% half span shows a considerably smaller suction level due to wing/body interference effects. Also at the inboard area still an increase in suction level beyond maximum lift can be seen. At the fixed wing, the suction peaks exhibit only minor changes from $\alpha = 18.5^\circ$ to $\alpha = 21^\circ$. In the aft portion of the fixed wing's upper side, the pressure coefficients are less negative, showing stronger pressure gradients towards the trailing edge. As the pressure side of the fixed wing is basically identical for both angles of attack, part of the lift breakdown of the configuration is attributed to the rear part of the fixed wing. The difference in total lift between both selected angles of attack amounts to 8 lcts. corresponding to about 3%. Finally, the pressure distributions at the slat feature a distinct decrease in the suction levels on the upper side in all sections. It is more pronounced in the midboard sections PS 4 and PS 6 indicating that the strongest loss in lift beyond maximum lift occurs midboards.

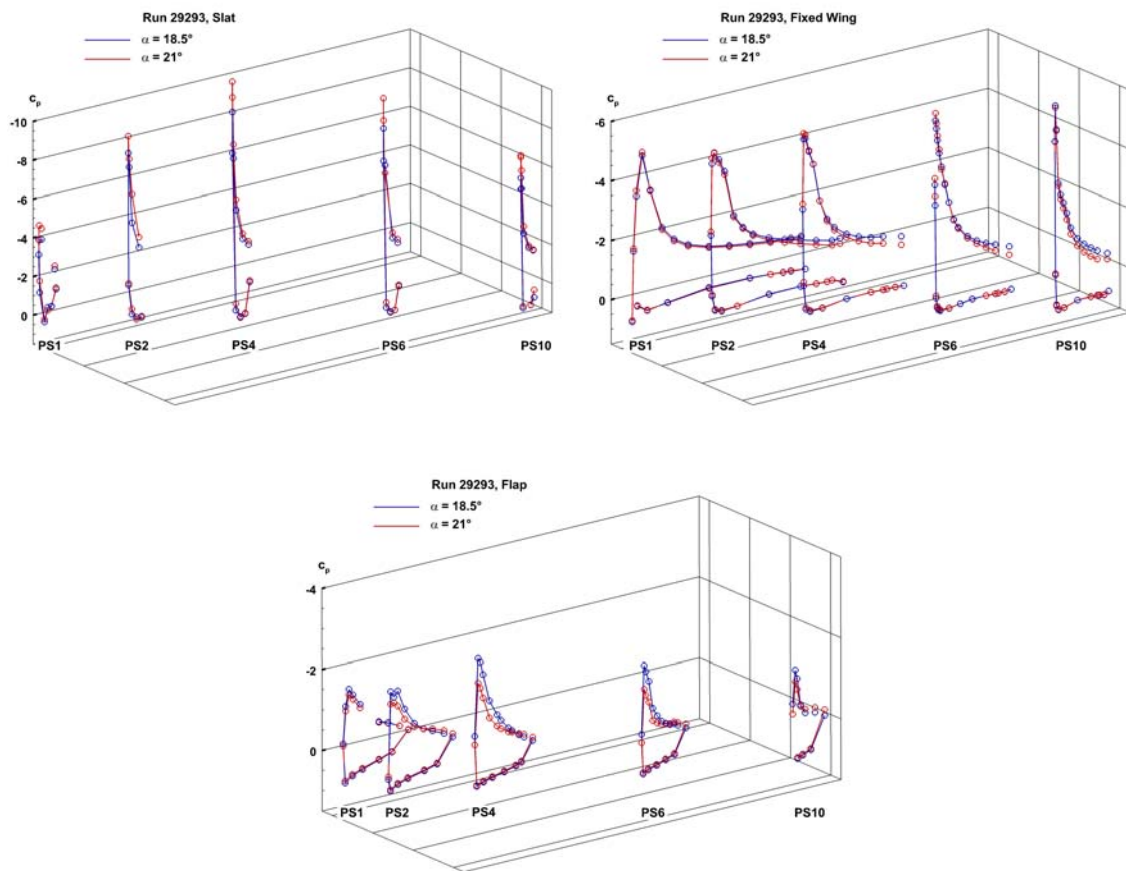


Fig. 4.5. Pressure distributions at and beyond maximum lift at low Re-number conditions

Due to the fact, that for the given model size and number of pressure taps, the pressure tube bundles had to be routed externally attached to the slat tracks. As this leads to a considerable blockage of the flow around the tracks and in the slat cove, the question about aerodynamic impacts arises. To investigate this, a specific test has been carried out with the tube bundles at the slat de-connected for all sections. The corresponding run is designated 29423. The de-connected tubes are shown for one track in Fig. 2.3, center photo. The lift curve, drag polar and pitching moment plots in Fig. 4.6, indicated by the red color, show that the tube bundles at the slat have a considerable aerodynamic effect in the upper lift regime. As mentioned above, the later run 29318 has been taken as a reference in this case due to consistency reasons. Without the tubes the maximum lift value amounts to $C_{L,max} = 2.70$ and is thus increased by 5 lcts.. The corresponding angle of attack is increased by one degree to $\alpha(C_{L,max}) = 20^\circ$. An influence becomes observable for $\alpha > 12^\circ$. Consistently, also the drag and the pitching moment are affected. While the total drag differs for lift values beyond $C_L = 2.5$, the more sensitive pitching moment reveals an impact for $C_L > 2.0$. In order to prove these differences, simplified quads of about the same blockage as the tube bundles have been attached to the slat tracks, also shown in Fig. 2.3, right photo. The results of this run, designated as 29424, show for lift, drag and pitching moment nearly the same results as for the configuration with the pressure tube bundles. It has to be considered, that these unexpected strong effects are linked to the specific model instrumentation/wing size combination, the low Reynolds number conditions, and a maximum lift layout, which is not limited by the slat. Therefore a generalization is hardly possible. Nevertheless, it underlines the sensitivity of maximum lift of a realistic three-dimensional aircraft configuration in wind tunnel testing.

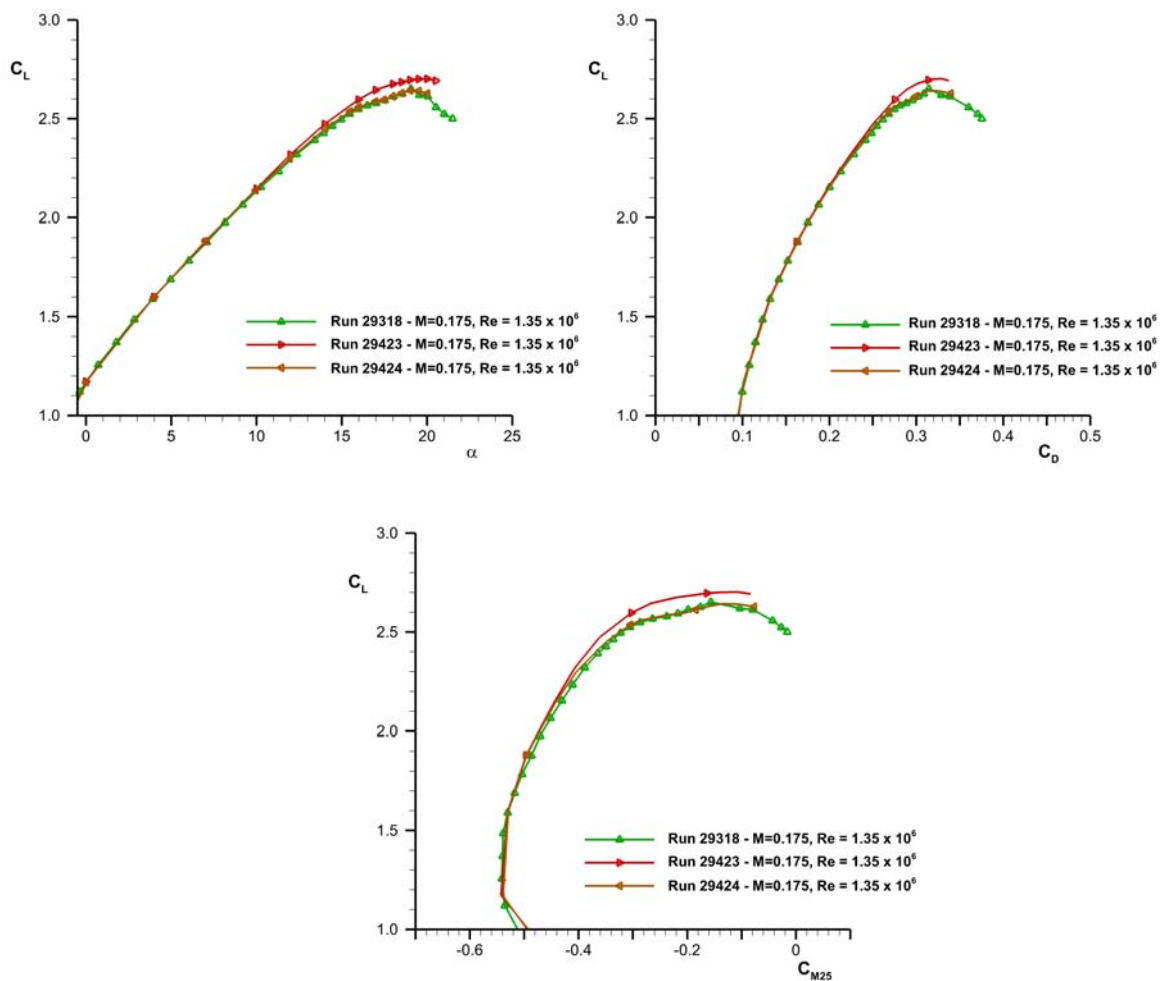


Fig. 4.6. Lift, drag, and pitching moment for the pressure tube bundle investigation at low Reynolds-number conditions

Oil Flow Visualization

Oil flow visualization is an appropriate means to investigate the appearance and extend of flow separation on the high lift wing and its elements. A large number of pictures has been taken during the wind tunnel test campaign from different perspectives. The photos depict the upper and the lower side of the high lift wing in different degrees of zoom. Fig. 4.7 shows as an example of view of the wing upper side from behind for angles of attack of $\alpha = 7^\circ$, 18.5° , and 21° . For $\alpha = 7^\circ$, widely attached flow is observed on the whole wing upper side. The wakes of the slat tracks and the attached pressure tube bundles are clearly visible. Starting from the wing kink a strong crossflow in outboard direction is detected on the outer flap. Close to the flap trailing edge separation trends are visible. When increasing the angle of attack to $\alpha = 18.5^\circ$ to maximum lift conditions, confined areas of separation appear on the fixed wing. They emanate from the wakes of FTF 5 and 7 and spread out laterally towards the trailing edge. The crossflow tendency on the flap appears to vanish. Beyond maximum lift at $\alpha = 21^\circ$, separation areas on the fixed wing further extend especially downstream of FTF 5. Also on the outer wing, downstream of FTF 9, a separation is developing. In summary, the strongest separation trends are found in the aft part of the midwing area at and beyond maximum lift.

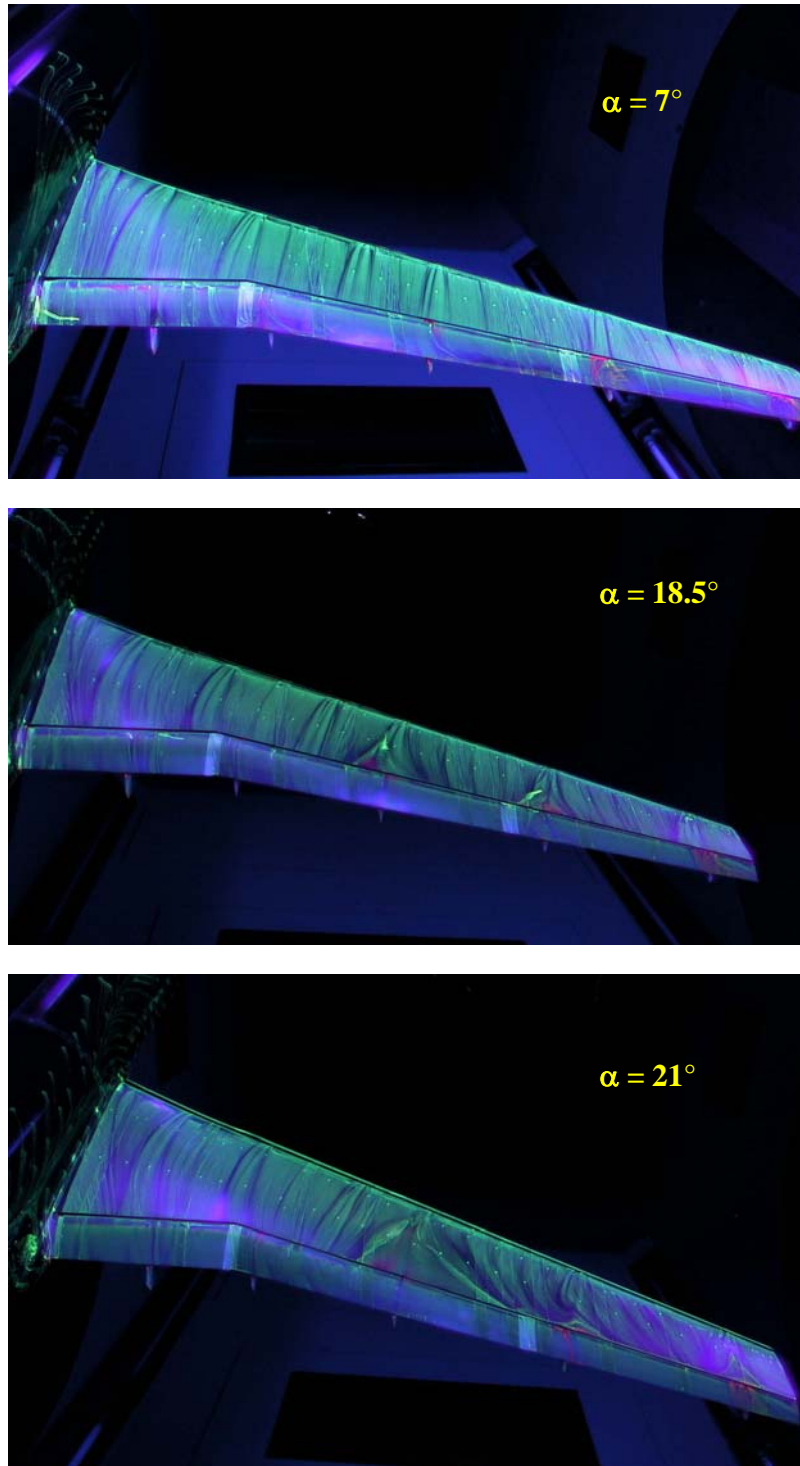


Fig. 4.7. Oil flow visualization for $\alpha = 7^\circ$, 18.5° , and 21° for low Re-number conditions

In order to assess the aerodynamic impact of the oil on the wing surface, the lift curve and drag polar have been evaluated, see Fig. 4.8. Applying oil to the wing causes a lift reduction of about 2 lcts. It has to be noted that the lift for $\alpha = 19^\circ$ is not available. The impact is rather limited to the lift regime around $C_{L,max}$.

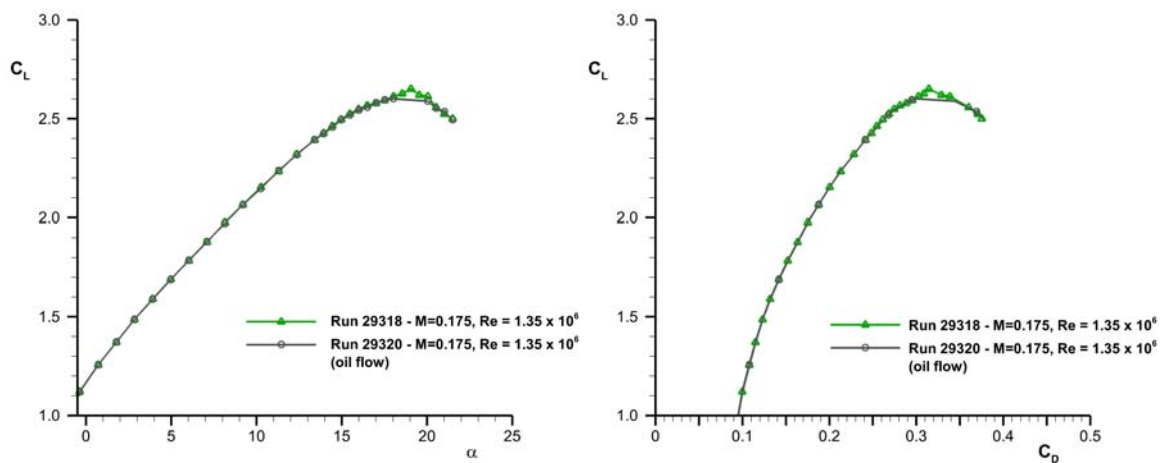


Fig. 4.8. Comparison of lift curve and drag polar for measurements with and without oil flow on the wing surface at low Reynolds-number conditions

The same holds for the drag polar where an increase in drag of about 20 dcts. is found for constant lift at $C_L = 2.6$. Thus, the influence of the oil on maximum lift is rather limited so that the oil flow pictures represent a consistent additional experimental evidence.

Particle Image Velocimetry

In addition to the surface measurements described above, also non-intrusive off-body flow measurements have been carried out using 2 and 3-component Particle Image Velocimetry (PIV). The measurement set-up and the location of the spanwise sections are described in chapter III. Basically, 2-dimensional vector plots with velocity information in a rectangular grid are available. As an example Fig. 4.9 depicts a time-averaged and an instantaneous velocity vector map for PIV plane 2 for an angle of attack close to maximum lift. The selected window d is above the fixed wing at about 75% local chord. The figure is taken from [7]. The wing surface is indicated by gray color beneath the velocity field. In both maps velocity vectors are displayed, with the velocity magnitude assigned to a color map. Indicated by light green and blue colors, the slat wake and parts of the fixed wing boundary layer become visible above the surface contour.

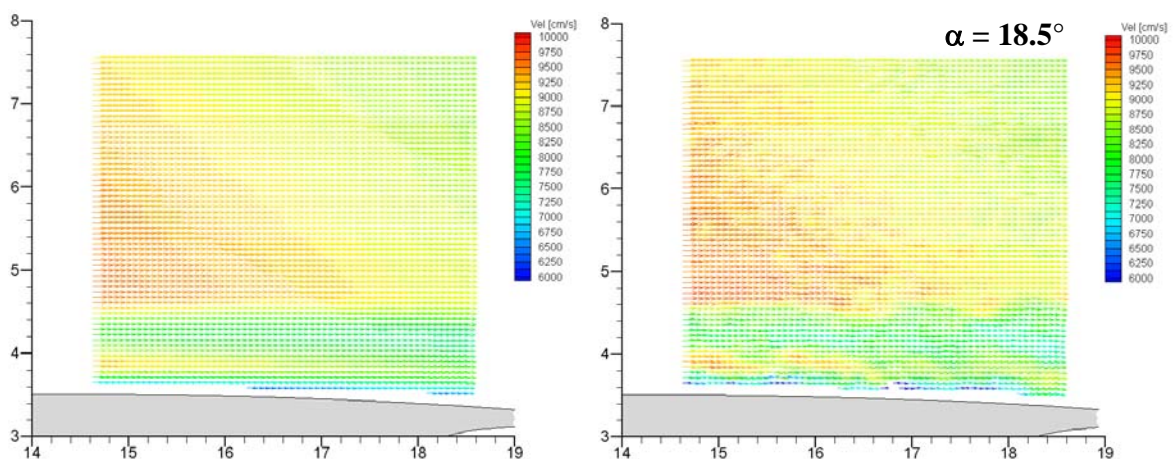


Fig. 4.9. PIV vector plot in plane 2, window d at $\alpha = 18.5^\circ$; Averaged PIV map (left hand side) and instantaneous map (right hand side).

In contrast to the time-averaged map on the left side with smooth area distributions, the instantaneous vector map reveals irregular edges of the slat wakes indicating unsteady motions with considerable velocities normal to the main flow direction. Due to the fact, that such velocity vector maps allow a qualitative analysis of the flowfield, the data have been further refurbished for the use in the 2nd phase of the High Lift Prediction Workshop. After transformation into the global coordinate frame, velocity profiles have been extracted to allow also a quantitative assessment and validation. Fig. 4.10 shows in the upper part the location of three evaluated windows and their location relative to the wing section together with the wall normal lines, along which the velocity has been evaluated.

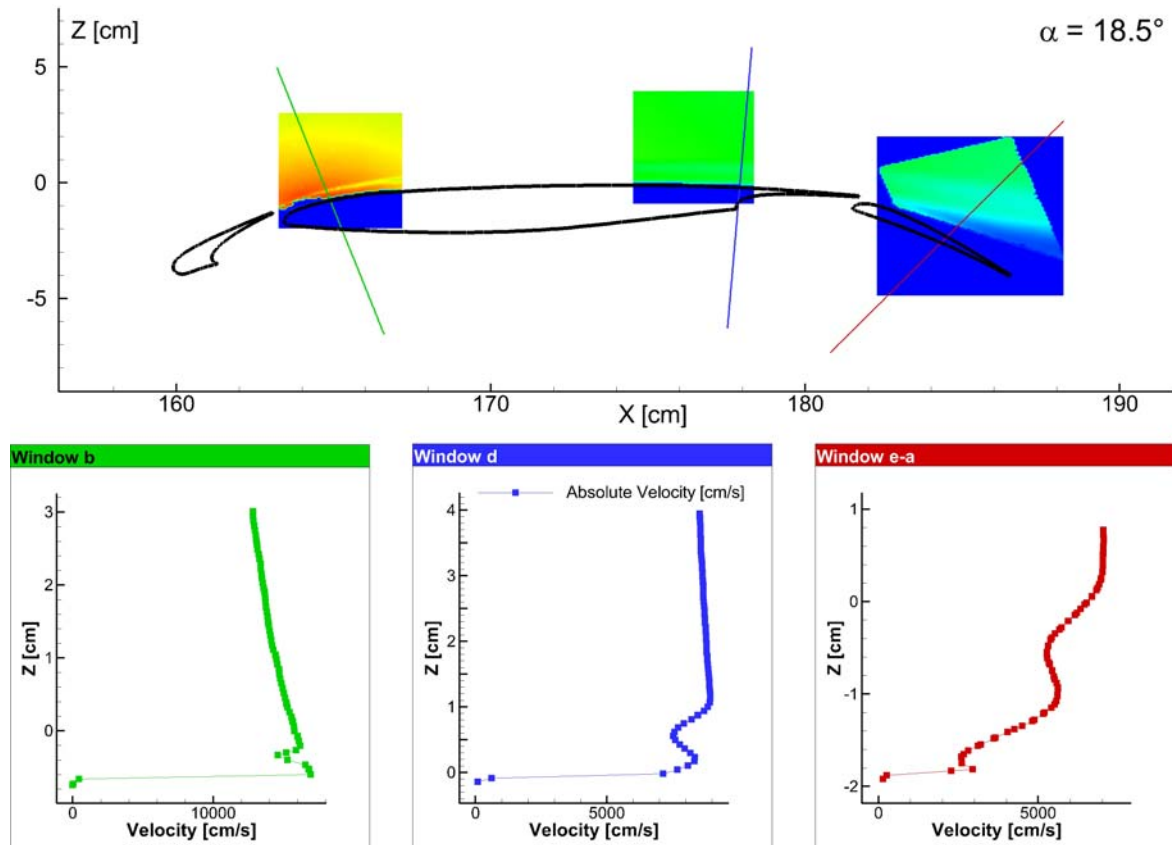


Fig 4.10. PIV windows b, d, and e and derived velocity profiles normal to the surface for low Reynolds number conditions in plane 2 at $\alpha = 18.5^\circ$

The velocity profiles are displayed in the lower part of the figure for all three extraction lines. The profile of window b behind the slat is characterized by the highest velocities. The slat wake is visible. The profile of window d above the rear part of the fixed wing shows a considerably reduced velocity level, which is still above the freestream velocity of 60 m/s (= 6000 cm/s). The wake of the slat is widened. In the profile that belongs to window e-a, the wake of the fixed wing and the slat wake are visible. A tendency of confluence between both wakes can be observed, as the flow between both wakes doesn't reach the level of the outer velocity.

Transition detection by Infrared Thermography and Hotfilm measurements

As described in chapter III, both techniques have been used simultaneously in order to have complementary information about the laminar to turbulent transition mechanisms. The analysis of the IR-images allows an aerial investigation of the transition location in a more qualitatively manner, while the results of the hotfilm measurements enable a comparatively precise detection of the transition with very limited spanwise extent.

Hotfilm arrays have been applied to the slat in three spanwise sections, see Fig. 3.2. For section 2, also the fixed wing leading edge is covered by a hotfilm. Fig. 4.11 shows two signal plots of the hotfilm on the slat, and the fixed

wing, respectively in section 2⁸. The ordinate shows the signals of the single hotfilms on the array vs. time, starting with the lower surface. Peaky signal distributions indicate transition. These kind of signal plots are the basis for the identification of transition locations for the specific angle of attack.

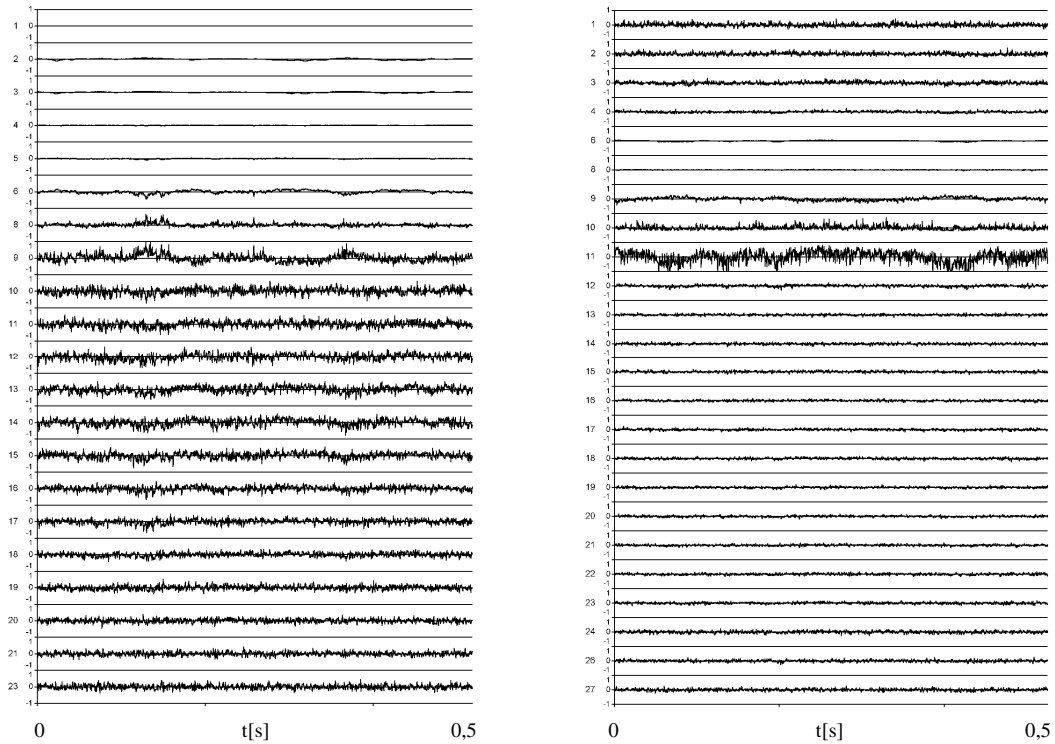


Fig. 4.11. Hotfilm signals in section 2 for low Re-number conditions, left slat (HF2, MR410), right fixed wing, (HF4, MR409) for $\alpha = 18.5^\circ$

In a subsequent step, an RMS-average of the signals is evaluated as depicted in Fig. 4.12. The abscissa characterizes the non-dimensional arclength of hotfilms on the respective wing element.

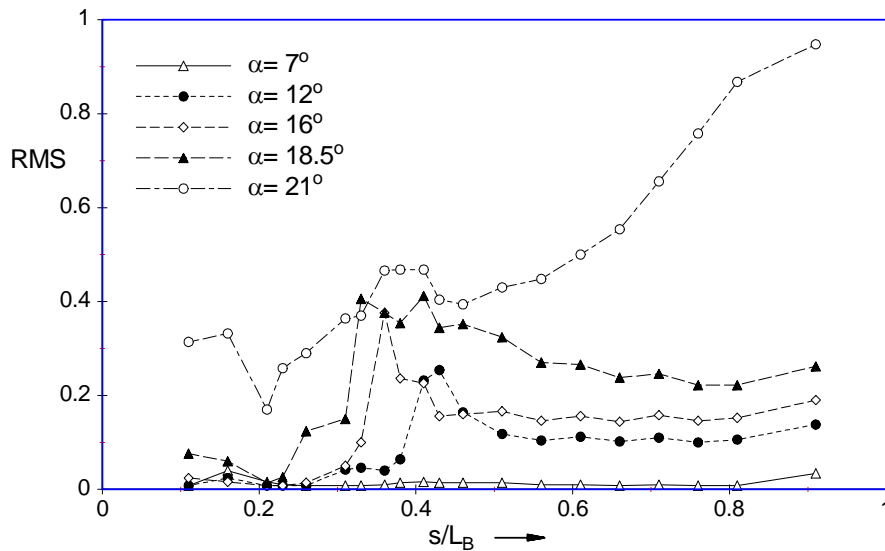


Fig. 4.12. RMS-evaluation of hotfilm signals vs. angle of attack for the slat in section 2 for low Re-number conditions

Thus, the development of transition vs. angle of attack can be identified. All hotfilm information has been compiled and analyzed for the various angles of attack and the four hotfilm arrays⁸. Fig. 4.13 shows the resulting transition locations and expected transition mechanisms for the slat and fixed wing in section 2. The locations of Tollmien-Schlichting transition, laminar separation, and attachment line transition are indicated vs. angle of attack.

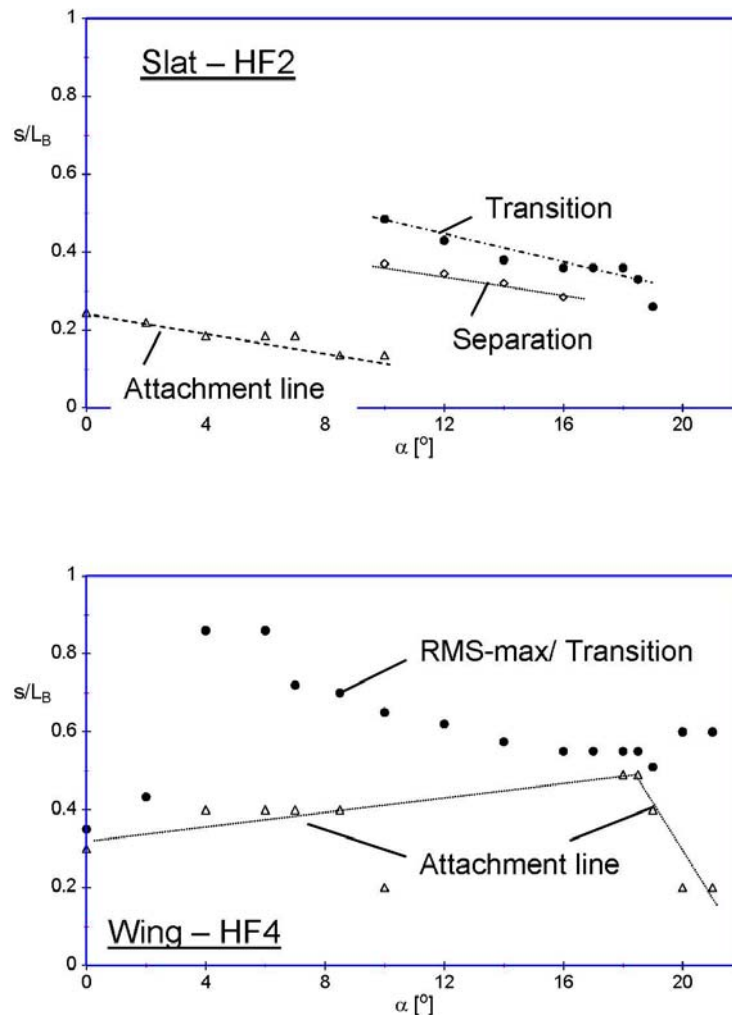


Fig. 4.13. Transition analysis of hotfilm signals vs. angle of attack for the slat and the fixed wing in section 2 for low Re- number conditions

Complementary to the hotfilm signals, IR-images have been recorded to further analyze the transition phenomena on the wing upper and lower surface. Fig. 3.1 depicts the three sections, which are photographed.

Fig. 4.14 shows as an example a series of 6 infrared pictures for increasing angles of attack for the considered configuration on the wing upper surface. Dark areas indicate regions with laminar flow. Especially on the slat laminar separation bubbles are expected, getting more pronounced with increasing angles of attack. Also wakes of the slat tracks are visible. A first interpretation of the transition phenomena is given by Hansen et. al. in Ref. 5. Both, the hotfilm signals and the infrared images will require further analysis and interpretation in order to provide comprehensive and conclusive guidance for the validation exercise scheduled in the 2nd phase of the High Lift Prediction Workshop.

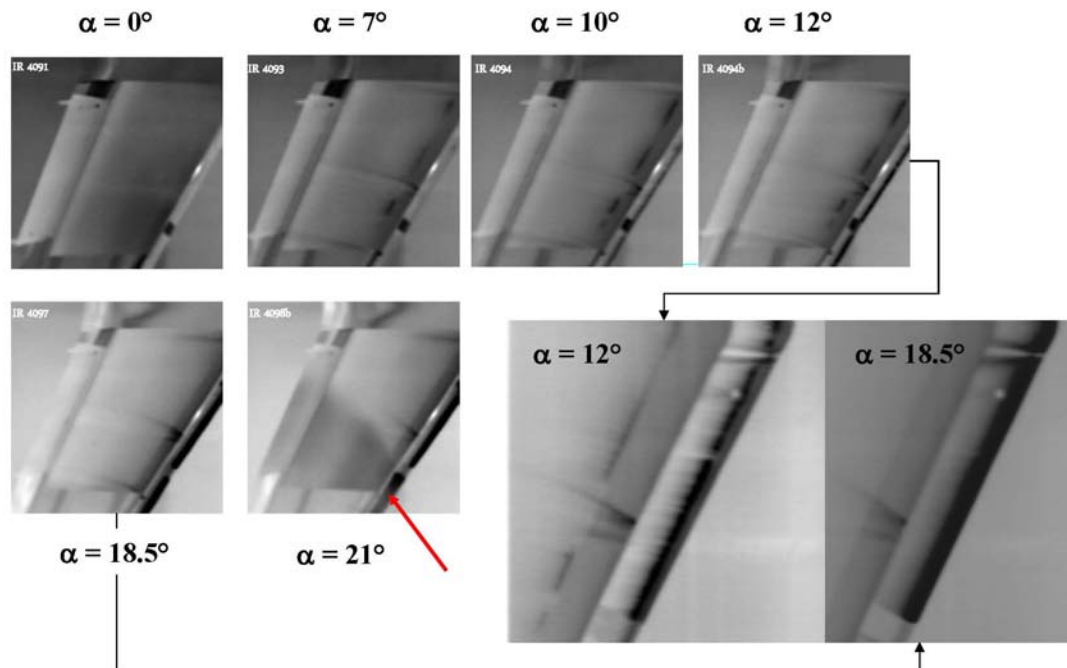


Fig. 4.14. Infrared images of the wing upper surface for 6 angles of attack for low Re number conditions

B. Experimental Evidence of the European Transonic Wind Tunnel, ETW

The experimental results for the DLR-F11 configuration discussed above underline the sensitivity of the flow and the possible impact of transitional phenomena. Therefore, it appears essential to supplement the database by corresponding experimental results at sufficiently high Reynolds number conditions, where these effects are supposed to play a minor role. The experimental results presented hereafter have been measured in 2002. The onflow parameters of the cryogenic test set-up are listed in table 5. For the present purpose the highest tested Reynolds-number of $Re = 15 \times 10^6$ has been selected, as it is fairly close to flight Reynolds-number for the type of aircraft configuration discussed here. The Reynolds-number is established by a combination of total pressure increase and total temperature decrease down to 115K. For this test campaign forces and moments and pressure distributions are available. The experimental results for this so-called high Reynolds number condition will be presented hereafter followed by a brief discussion of scaling effects in the range of intermediate Reynolds-numbers.

Forces and Pitching Moments

The corresponding reference run for the high Reynolds number conditions in the ETW is designated Run 238. Fig. 4.15 shows a comparison of the lift curve, drag polar, and pitching moment distribution for the positive angle of attack range. When comparing the slope of the various curves it should be taken into account that the angle of attack resolution of the ETW results is significantly higher. In the results of the ETW, only every fourth angle of attack is evaluated in the plot. The higher Reynolds number leads to an increase in lift over the whole range of angles of attack. At $\alpha = 7^\circ$ the difference amounts to 5 lcts. and increases up to 25 lcts. at maximum lift. The corresponding angle of attack increases from $\alpha(C_{L,max}) = 19^\circ$ to about 20.5° for $Re = 15 \times 10^6$. The lift breakdown after $C_{L,max}$ is more pronounced for the high Reynolds-number case. The drag polar for the high Reynolds number fully encloses the one for the low Reynolds number conditions. As expected, drag is lower for the ETW results for the whole range of lift coefficients. The difference in drag amounts to about 90 dcts. at $CL = 1,17$ and increase to about 460 dcts. close to maximum lift. The pitching moment curve reflects the general behavior of the low Reynolds number case. Nevertheless, pitching moment is more negative for the whole polar corresponding to the higher lift generation. The trend to increase negative pitching moment at the highest measured angles of attack is also found in the ETW

results, being much more pronounced than for the results of the B-LSWT, as for the ETW the range of angles of attack beyond maximum lift is considerably larger.

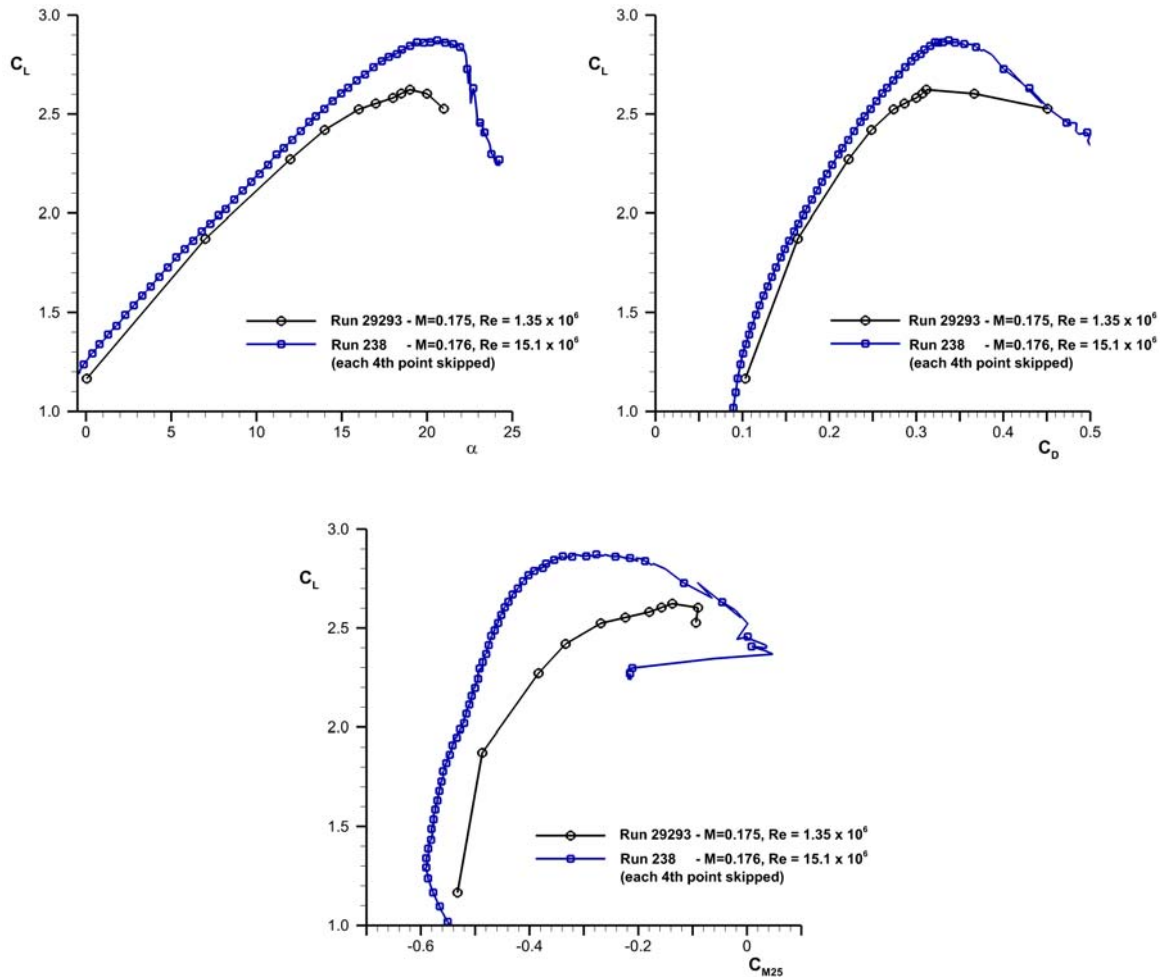


Fig. 4.15. Lift, drag, and pitching moment for low and high Reynolds-number conditions

In order to assess the comparability of the experimental results measured in two facilities with the same model a back-to-back comparison is attempted. For this purpose, the lowest Reynolds number measured in the ETW in the present context, $Re = 1.46 \times 10^6$, is selected in order to compare the ETW results to the B-LSWT results. Fig. 4.16 shows corresponding plots for the lift curve, the drag polar, and pitching moment. Results measured in the ETW are marked by blue colors. In addition to the high Reynolds number run 238, which is also shown, run 197 marks the condition which comes closest to the B-LSWT onflow conditions. The Mach-number amounts to $M = 0.177$ and the Reynolds number to $Re = 1.46 \times 10^6$. Given the fact, that the Reynolds number is still about 7.5% higher than the one in the B-LSWT, a very satisfying agreement in the lift curve and drag polar is obtained, when comparing the corresponding blue graph (diamonds) and its black counterpart (circles). The deviations lie well within the band that has been observed when analyzing some spurious effects for the B-LSWT tests. The blue lift curve confirms, that the early deviation from the linear lift increase is indeed related to the low Reynolds-number condition and not a facility or model issue. The same holds for the more moderate lift breakdown, which is also reproduced by the ETW test results for the low Reynolds-number. As expected the deviations in pitching moment are larger between the two low Reynolds-number datasets, with the ETW results are exhibiting a more negative pitching moment. The lift match being quite satisfying underlines the impact that small deviations in the pressure distributions can have on the pitching moment. Identifying the specific reason for these deviations would require a detailed analysis of the pressure distributions for both low Reynolds number results, which is beyond the focus of the present paper.

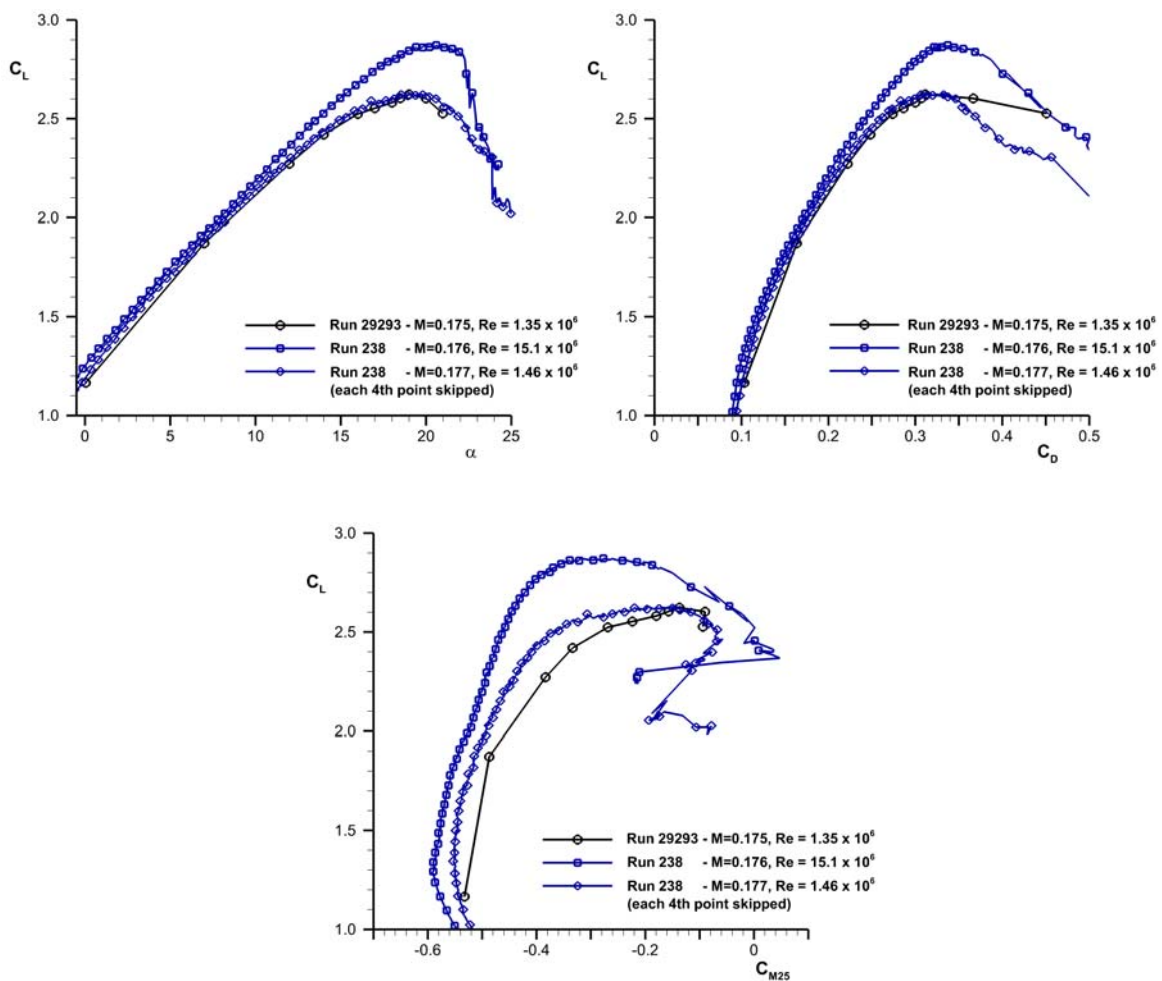


Fig. 4.16. Lift, drag, and pitching moment for low and high Reynolds-number conditions in the ETW

Pressure Distributions

The analysis of the pressure distributions is done according to what has been presented in the section for the low Reynolds number results. In order to assess the Reynolds number effects in the pressure distributions, the results from the low Reynolds number tests have been compared to those of the high Reynolds number conditions. For this comparison, pressure section PS 4 at $\eta = 0.449$ has been selected and, in contrast to the pure low Reynolds number assessment, pressures section PS 6 at $\eta = 0.681$, as the pressure data for section 10 are rather incomplete. It has to be taken into account, that also the same angles of attack with $\alpha = 18.5^\circ$ and $\alpha = 21^\circ$ have been analyzed. While this offers the advantage of having directly comparable incidences, it has at the same time the drawback that for the high Reynolds number conditions, $\alpha = 21^\circ$ is directly a maximum lift condition, where lift breakdown is still about to occur.

The comparison of the pressure distributions is shown in Fig. 4.17 for the midboard section. Low Reynolds number results are indicated by solid lines, high Reynolds number results by dashed lines. The angles of attack are marked by different colors. Consistent with the lift curves in Fig. 4.16, the differences due to the increase of Reynolds number by about an order of magnitude a quite small for the lowest angle of attack. For $\alpha = 18.5^\circ$, the differences become more pronounced, especially on the slat. These differences increase for the highest angle of attack with the strongest effects visible on the slat and the flap. Although $\alpha = 21^\circ$ is close to maximum lift for the high Reynolds number condition, the flap reveals the same trend of having a lower suction levels on the upper

surface at $\alpha = 21^\circ$ compared to $\alpha = 18.5^\circ$. This indicates, that the general mechanism for the lift breakdown is maintained also for higher Reynolds number conditions.

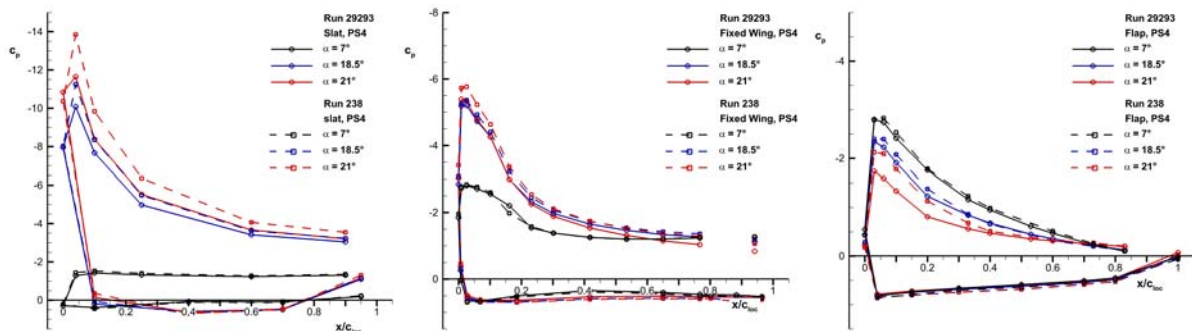


Fig. 4.17. Midboard pressure distribution PS4 at different angles of attack, comparison of low and high Re-number conditions

The pressure distributions at the outboard section PS 6 in Fig. 4.18 confirm these trends on all three elements. In general, the suction levels are higher than for the inboard section in Fig. 4.17. Again, the suction peaks on the slat increase continuously with increase angle of attack, while a lift breakdown starts at the flap for $\alpha = 21^\circ$ for low as well as for high Reynolds number conditions.

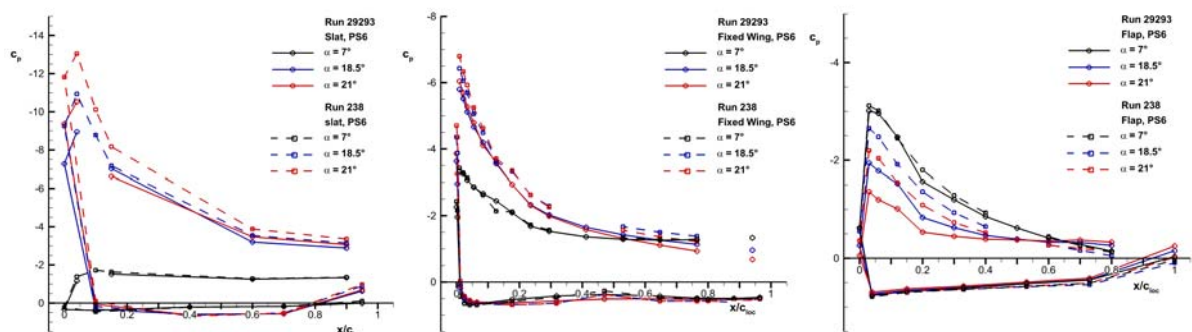


Fig. 4.18. Outboard pressure distribution PS6 at different angles of attack, comparison of low and high Re-number conditions

To underline these findings, an assessment of the spanwise development of the lift generation is depicted in Fig. 19 at pressure sections PS1, PS2, PS4, PS6, and PS 10 in a three-dimensional view exclusively for high Reynolds number conditions. Starting with the slat, the most pronounced increase in suction peaks when moving from $\alpha = 18.5^\circ$ to $\alpha = 21^\circ$ occurs midboards. The corresponding changes on the fixed wing are comparatively small. In all sections a slightly higher pressure level is reached at the trailing edge with overall increased pressure gradients from fixed wing leading to trailing edge. The pressure distributions on the flap confirm that the trends observed on Fig. 4.17 and Fig. 4.18 hold for all considered sections along the span with increasing tendency towards the flap tip.

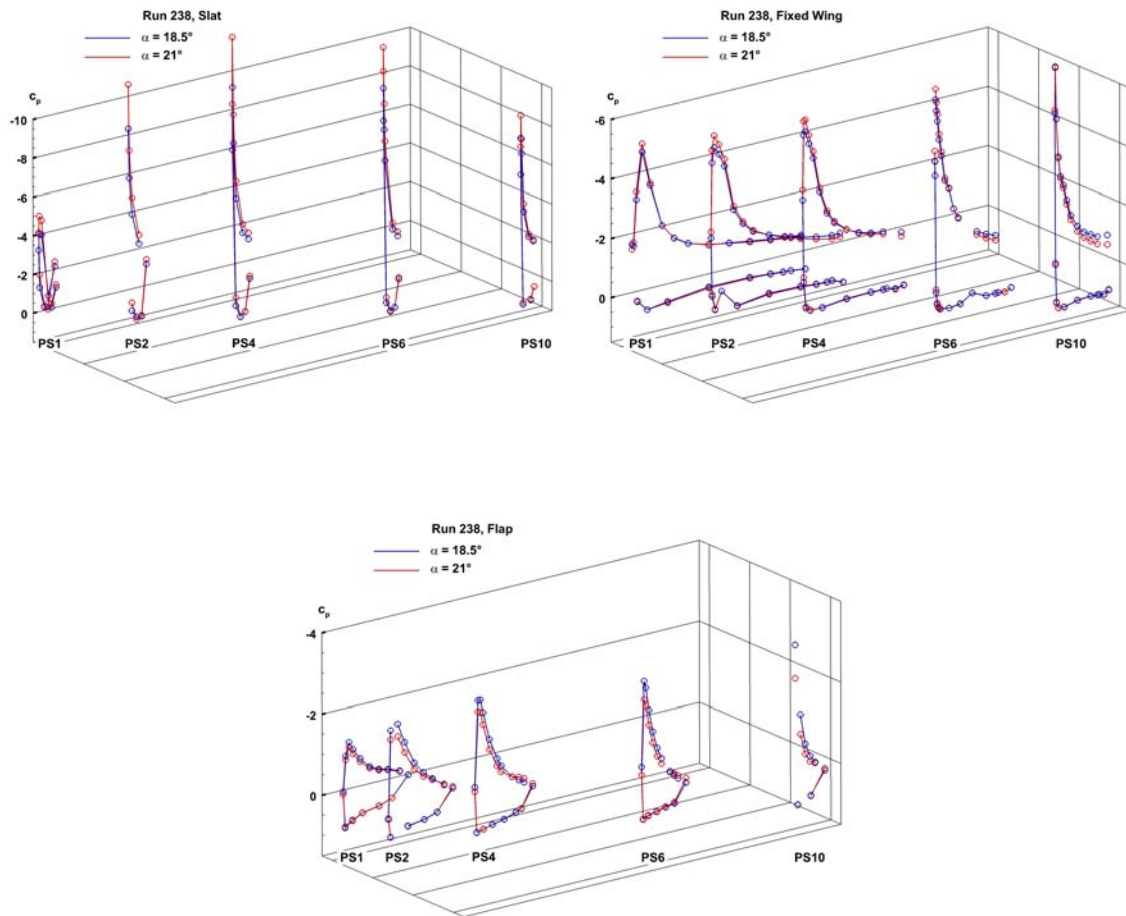


Fig. 4.19. Pressure distributions at and beyond maximum lift at low Re-number conditions

Reynolds number scaling trends

Making use of the data published in Ref. 3 for the considered configuration, an assessment of the Reynolds number scaling effects shall be outlined. Fig. 4.20 shows the development of the maximum attainable lift vs. Reynolds number in the range between $Re = 1.45 \times 10^6$ up to $Re = 15 \times 10^6$. Increasing Reynolds number leads to favorable scaling effects for the whole considered range. The largest increase in maximum lift is occurring for $1.5 \times 10^6 < Re < 4 \times 10^6$. For large Reynolds numbers the increase in lift is much more moderate at a nearly linear gradient of about $\Delta(C_{L,max}) / \Delta(Re) = 0,0065$.

As reported in Ref. 3 unfavorable effect have been observed for the DLR-F11 model, but are related to engine/airframe interference phenomena for the configurations with installed through-flow-nacelles.

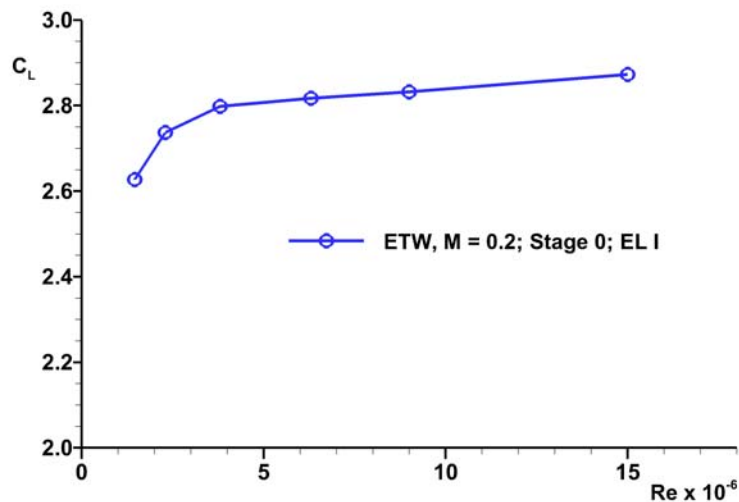


Fig. 4.20. Reynolds number scaling effect measured for the DLR-F11 configuration in landing setting in the ETW for $M = 0.2$

V. Conclusion and Outlook

Experimental evidence for the DLR-F11 high lift configuration to be used within the context of the 2nd phase of the AIAA High Lift Prediction Workshop is presented and analyzed. The wing/body model geometry, featuring a continuous slat and flap system in landing setting, is representative for a wide-body commercial aircraft. A CAD model in various degrees of detail has been refurbished, serving as the common geometrical basis for the scheduled CFD investigations. Experimental data of the European project EUROLIFT for low and high Reynolds number conditions have been made available. The data for low Reynolds numbers have been gathered in the Low Speed Wind Tunnel of Airbus in Bremen, B-LSWT, while the high Reynolds-number condition data have been measured in the European Transonic Windtunnel, ETW, under cryogenic conditions. The Reynolds numbers between both datasets differ by an order of magnitude. The comparison of the force and moment data for low and high Reynolds number conditions shows the expected trends due to the typical reduction of viscous effects. The lift breakdown is triggered in both cases by the aft part of the center wing and the flap. A back-to back comparison between both tunnels for comparable low Reynolds number shows a good overall agreement in overall lift and drag, confirming the effect due to the increase in Reynolds-number. Reynolds number scaling effects are favorable for the considered wing/body configuration.

In addition to force and moment data, a comprehensive validation database is presented from the atmospheric low Reynolds number tests. The experimental data comprise oil flow pictures, transition information by hotfilms and infrared thermography, as well as PIV velocity data in various locations of the F11 configuration for a sample of angles of attack up to and beyond maximum lift. Examples of the oil flow pictures, transition information, and off-body velocity data are presented. They underline the suitability of the presented database for CFD validation purposes.

Both, the hotfilm signals and the infrared images require some further analysis and interpretation in order to provide comprehensive and conclusive guidance for the validation exercise scheduled in the 2nd phase of the High Lift Prediction Workshop. Out of the full database the organizing committee of the High lift Prediction Workshop will select suitable onflow conditions and experimental evidence for the validation exercise.

Acknowledgments

The modification of the windtunnel model and the experimental data of the B-LSWT and the ETW, provided for the 2nd High Lift Prediction Workshop, are co-funded by the European Commission through the research project EUROLIFT under contract No. G4RD-CT-1999-00072 of the 5th framework programme and the consortium of the EUROLIFT project.

The authors are grateful to both parties for releasing the data for a broader international use. Special thank go to the windtunnel teams in the Bremen Low Speed Wind Tunnel and the ETW for their excellent work. We are very grateful to the specialists for the various test techniques, namely Klaus-Peter Neitzke and Heinz Hansen of Airbus-Operations, as well as Hans-Peter Kreplin and the PIV team of DLR, for their support in searching and providing documents and interpreting the datasets after quite a long period of time.

Finally, all partners of the EUROLIFT consortium, namely Airbus-Germany (DASA GmbH), Airbus-France (Aerospatiale Matra-Airbus), Alenia Aeronautica, CASA, CIRA, Dassault Aviation, ETW (European Transonic Windtunnel GmbH), DLR, FOI, IBK (Ingenieurbüro Dr. Kretschmar), INTA, NLR, and ONERA are acknowledged for their support in releasing the data.

References

- ¹ J. Slotnick, J. Hannon, M. Chaffin, "Overview of the 1st AIAA CFD High Lift Prediction", 49th Aerospace Sciences Meeting, Orlando, FL, 05 – 07 January 2011, AIAA 2011-0862 (2011)
- ² R. Rudnik, P. Thiede, "European Research on High Lift Aircraft Configurations in the EUROLIFT Projects" CEAS/KATnet Conference on Key Aerodynamic Technologies, CP, 2005, pp. 16.1-16.8.2005 (2005)
- ³ R. Rudnik, Germain, E., "Reynolds-Number Scaling Effects on the EUROPEAN High Lift Configurations", Journal of Aircraft, Vol. 46, No. 4, July-August 2009, pp. 1140-1151. (2009)
- ⁴ Rudnik, R., "Stall Behaviour of the EUROLIFT High Lift Configurations", 46th AIAA Aerospace Sciences Meeting and Exhibit, Reno, NV, 7 – 10 January 2008, AIAA 2008-0836 (2008)
- ⁵ H. Hansen, P. Thiede, R. Rudnik, F. Moens, J. Quest, "Overview about the European High Lift Research Programme EUROLIFT," AIAA 2004-767 (2004)
- ⁶ Kompenhans J., Raffel M., Dieterle L., Dewhirst T., Vollmers H., Ehrenfried K., Willert C., Pengel K., Kähler C., Schröder A., Ronneberger O., "Particle Image Velocimetry in Aerodynamics: Technology and Applications in Wind Tunnels", J. Visualisation, Vol. 2, pp. 229 -244, 2000
- ⁷ A. Arnott, J. Kompenhans, G. Schneider, J. Agocs, B. Sammler, A. Schröder, "PIV Experiments in the Low Speed Wind Tunnel of Airbus Bremen, Germany", EUROLIFT Project Report TR 1.3.1-8, 2003
- ⁸ H.-P. Kreplin, DLR, Institute of Aerodynamics and Flow Technology, Göttingen, personal communications, 2012